

AD-A273 157



12

# Investigation of Raman Beam Cleanup and Phase Conjugation

## Final Report

for

Period May 1, 1989 - April 16, 1993

Prepared by:

Rita Mahon, Ph.D.

JAYCOR

Applied Physics Division  
1608 Spring Hill Road  
Vienna, Virginia 22182-2224



Submitted to:

Director

Naval Research Laboratory  
4555 Overlook Avenue, S.W.  
Washington, DC 20375-5000

Contract Number: N00014-89-C-2146

November 5, 1993



93-28296

4218

This document has been approved  
for public release and sale; its  
distribution is unlimited.

TEM-01254

93 11 17 017

# **Investigation of Raman Beam Cleanup and Phase Conjugation**

**Final Report  
for  
Period May 1, 1989 - April 16, 1993**

**Prepared by:**

**Rita Mahon, Ph.D.**

**JAYCOR  
Applied Physics Division  
1608 Spring Hill Road  
Vienna, Virginia 22182-2224**

**Submitted to:**

**Director  
Naval Research Laboratory  
4555 Overlook Avenue, S.W.  
Washington, DC 20375-5000**

**Contract Number: N00014-89-C-2146**

**November 5, 1993**

**Best Available Copy**

## Table of Contents

Introduction	Page 1
Multiple pulse effects on Raman gain	Page 1
Second Stokes generation	Page 5
Imaging through a low light level Raman amplifier	Page 8
Competition between signal and noise in narrowband Raman amplifiers	Page 16
Applications of quantum limited imaging to time gated imaging through scattering media	Page 19
Imaging through scattering media	Page 23
Imaging through tissue with time-gated optical systems	Page 31
Real-time imaging of debris in oil	Page 34
References	Page 37

DTIC QUALITY INSPECTED 8

Accession For	
NTIS CRA&I	<input checked="" type="checkbox"/>
DTIC TAB	<input type="checkbox"/>
Unannounced	<input type="checkbox"/>
Justification	
By	
Distribution /	
Availability Codes	
Dist	Avail and / or Special
A-1	

## Introduction

During the course of the contract period 1990-1993 the basic science studies of the transient Raman effect have been completed and questions concerning the growth of the Stokes signal from noise and the influence of quantum noise on low light level amplification, have been studied. The program has evolved into an imaging program using the Raman amplifier as a low noise, high gain, optical amplifier. In this capacity, extensive measurements have been made on characterizing the optical transport through turbid media, with a particular emphasis on the parameter space common to human tissue. A separate program has evolved which does not use the Raman amplifier, but requires innovative recognition-imaging devices to detect debris in engine or gear box oil on a real-time basis.

In this report we will discuss the experiments which have been conducted and the conclusions drawn from the data. The main lasers used for this work have been a 30 psec mode-locked Nd:YAG, a 10 nsec seeded-oscillator Nd:YAG, and some pulsed near infra-red diode lasers. A 2 psec resolution streak camera was available for all the experiments. A gated intensified camera was used for the earlier imaging experiments while a 16 bit cooled CCD camera was used for the later imaging work. The specific experimentals are variations of the basic Raman amplifier system first described in reference 1.

There are seven main topics which will be discussed in detail in this report:

1. Multiple pulse effects on Raman gain
2. Higher order Stokes generation
3. Quantum limited imaging
4. Competition between signal and noise in narrowband Raman amplifiers
5. Imaging through turbid media
6. Application to tissue imaging
7. Real-time imaging of debris in oil

### I. Multiple Pulse Effects on Raman Gain

Due to the fact that the phonon field in the Raman medium can retain the phase that has been produced by a transient interaction, subsequent pulses that interact in that same medium can have modified gain characteristics. This is certainly true if the pulses in question are much shorter than the  $T_2$  time in the medium and if multiple pulses interact before a full  $T_2$  time period has elapsed. This could also be true even if the pulses are separated by multiple  $T_2$  times. In either case, the key to the effect is that the phonon field in the medium that has been created by the interaction of the first pump and seed-Stokes pulses is not completely lost due to dephasing collisions and can act as a 'jump-start' for the interaction in a subsequent pulse.<sup>2-7</sup>

We have performed a series of experiments to study the effects of multiple, closely spaced pulses interacting in a Raman medium. One set of experiments studied the enhanced gain that could be achieved for the subsequent seed-Stokes pulses in a train, and another set studied the gain that resulted when the phase of every seed-Stokes pulse in the train alternated by  $\pi$ .

The modification to the experimental apparatus for these experiments consisted of inserting a series of partial reflectors after the doubling crystal in such a manner that either 4 or 8 pump pulses, with approximately equal amplitudes, were produced. The separation between the pulses could be adjusted from between zero to approximately 1500 psec. These pulses were then used to generate a train of seed-Stokes pulses and were also used as the pump pulses to the amplifier cell. Multiple pulse effects in the seed-Stokes generating cell were minimized by having a high gain in the cell and allowing all pulses to grow into the pump depletion regime. In some of the experiments it was necessary to reverse the phase of every other seed-Stokes pulse. That was accomplished by the use of an electro-optic crystal driven by a radio-frequency voltage signal. The voltage applied to the crystal caused an alternating delay and advance of  $\pi/2$  in alternating pulses.

Figure 1 gives a schematic representation of the type of interactions that were studied. The fields of idealized pump and Stokes pulses that are incident on the amplifier cell are shown. The pulses are assumed to be separated by less than the  $T_2$  time of the medium, so the phonon field that grows from the interaction during one pulse duration, while undergoing some decay, is still present at the start of the next pulse, as is shown. Figure 1(a) presents the case where all of the seed-Stokes pulses are the same phase. There the phonon field grows from pulse to pulse until a steady-state condition is reached. That steady-state condition is reached when the decay of the phonon field between pulses is just compensated for during the next interaction. The amplified Stokes field is also shown. Without the enhancement in gain from pulse to pulse created by the residual phonon field, each pulse would simply see the gain shown for the first pulse of the train.

Another type of interaction during the pulse train is illustrated in Fig. 1(b). The same conditions apply as in Fig. 1(a), except that the phase of every other pulse in the seed-Stokes pulse train has undergone a  $\pi$  phase shift in relation to the other pulses in the train. The effect of that phase reversal is to cause the energy in the phonon field that is left over from one interaction to feed back into the interacting light fields. Since the phonon field has suffered some decay due to dephasing collisions, the phonon field in the next interaction can be reduced and driven through zero. In that case, the phonon field will grow to some level with the opposite phase that it started with. Because of the alternating nature of this interaction, the amplified Stokes field does not build up in gain as it did when all pulses had the same phase.

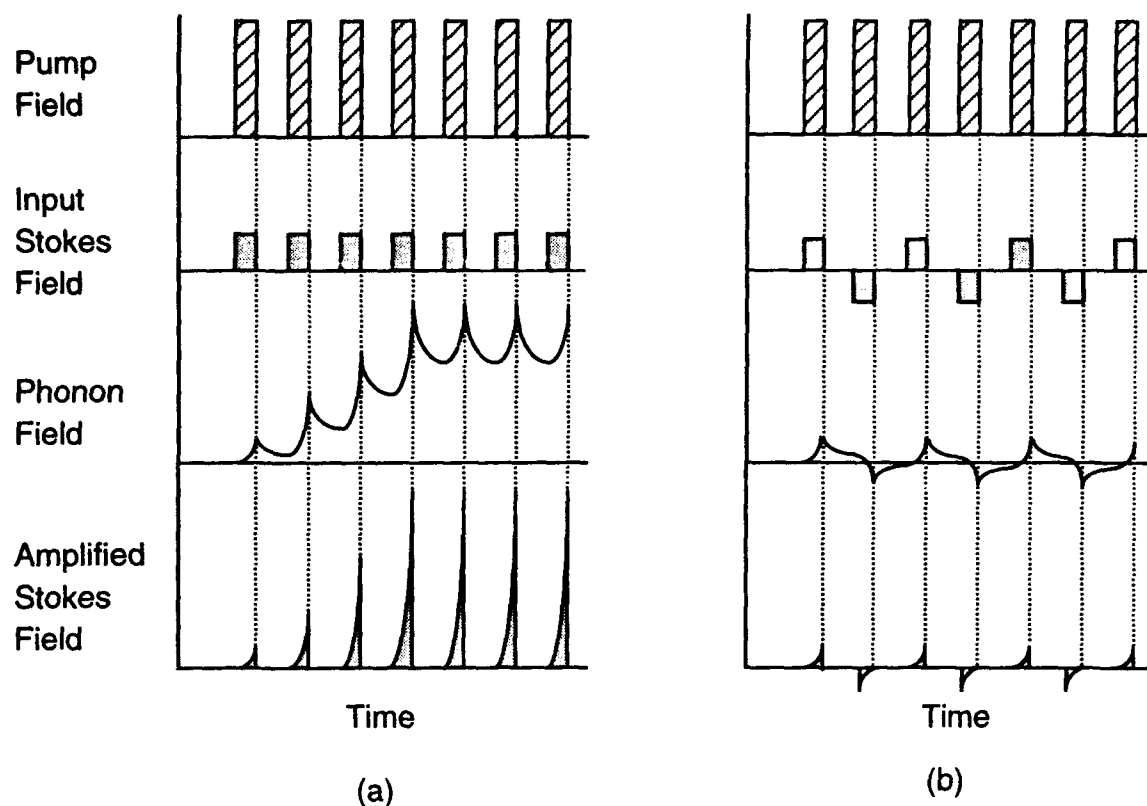


Figure 1. Schematic illustration of Raman gain buildup in a pulse train. The seed-Stokes pulses have a constant phase in (a), and a phase that alternates by  $\pi$  for every pulse in (b).

Figure 2 illustrates experimental data that was obtained with four pulses for the case when all of the seed-Stokes pulses had a uniform phase during the pulse train. The interacting pulses had a duration of approximately 40 ps and the separation between pulses was 100 ps. The  $T_2$  time in this case was 300 ps, so the phonon field that was generated decayed only a small amount between pulses. The ratio of the energy of the seed-Stokes pulses to the pump pulses was  $10^{-8}$ . The left-hand bar in each set shown in Fig. B shows the relative energy of the seed-Stokes pulses and the right hand bar in each set shows the relative energy in the amplified pulses. The energy of the first seed-Stokes pulse was approximately one-tenth the energy of the other seed-Stokes pulses due to the way it was generated in the seed-Stokes cell. As the size of that first amplified pulse indicates, the single pulse gain in this particular configuration was about 20. Because of the phonon field that was left over between pulses, however, the overall gain in the pulse train was over  $10^5$ . Data that was taken with pulses spaced farther apart in time confirmed that the overall pulse-train gain was lowered as the separation between pulses was increased. This overall gain was lowered to a value equal to the single pulse gain when the pulses were separated by approximately 4  $T_2$  times. This number is consistent with calculated values.<sup>4</sup>

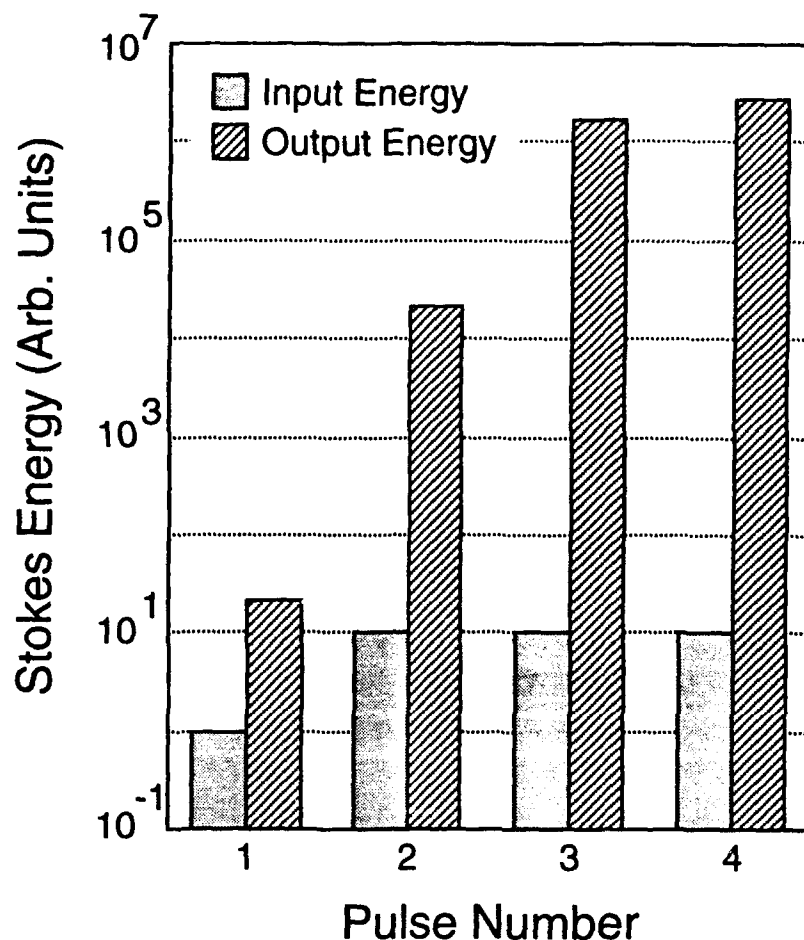


Figure 2. Measured amplification of individual pulses in a pulse train. The left hand bar in each pair indicates the seed-Stokes intensity, while the right hand bar indicates the amplified-Stokes intensity. The pulse repetition time was 100 ps and the dephasing time  $T_2$  was 300 ps. The incident-Stokes intensity was approximately  $10^{-8}$  of the pump intensity.

Figure 3 shows experimental data on the stimulated Raman gain from a pulse train of eight pulses with both uniform and alternating phases on the seed-Stokes pulses. The ratio of pulse separation to the  $T_2$  time was 1.8, so in these cases the pulse separations were longer than the  $T_2$  time. Curve (a) shows the gain experienced by a uniform phase pulse train. The gain is very small on the first three pulses, and then the gain grows to approximately 100. Curve (b) shows the gain experienced by a pulse train in which the seed-Stokes pulses were given an alternating  $\pi$  phase difference. Up until the fourth pulse the gain is approximately the same as for that of the uniform phase pulse train, but after that the gain varies widely and oscillates with a period of two pulses. This is a clear experimental demonstration of the modification in gain that occurs when the phasing of

alternate seed-Stokes pulses is such that it opposes the phase of the left over phonon field in the medium.

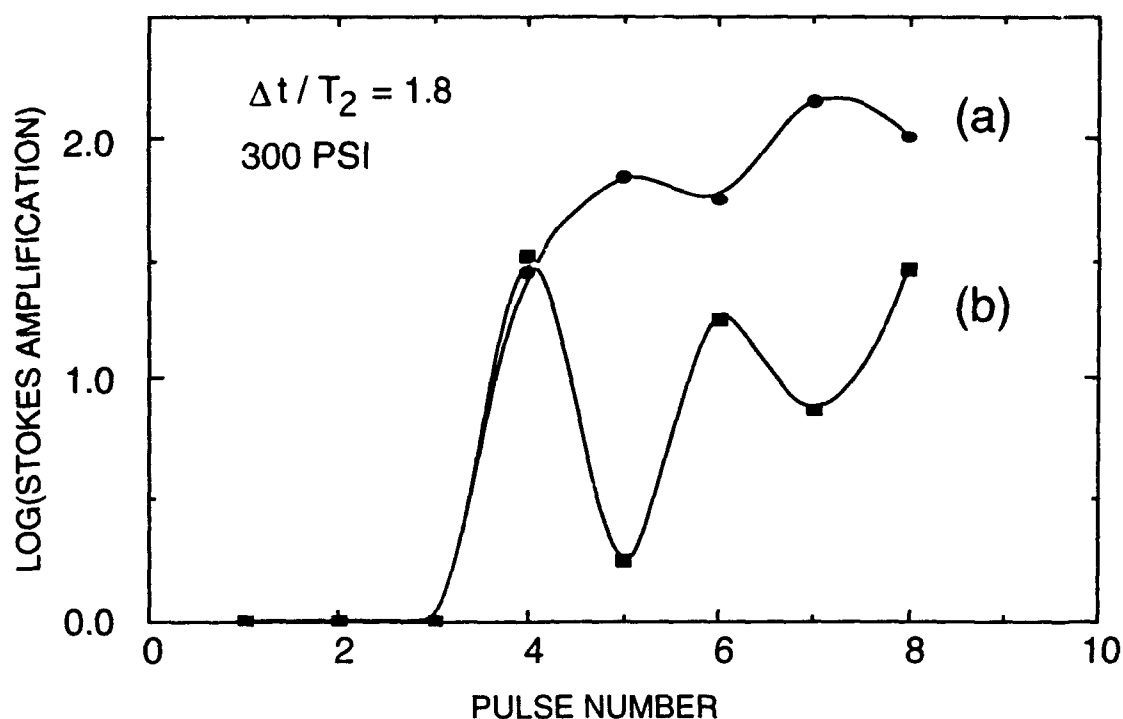


Figure 3. Measured amplification of individual pulses in a pulse train for the case of uniform seed-Stokes pulse phase (a), and alternating seed-Stokes pulse phase (b). This data was taken in hydrogen gas at 300 psi, giving a  $T_2$  time of approximately 250 ps. The pulse separation was 450 ps, giving  $\Delta T/T_2 = 1.8$ .

Theoretical calculations of the gain that would be expected in all of the above cases gives qualitative agreement with the results shown in Figs. 2 and 3. Detailed comparison between experiment and theory is difficult, however, because of the uncertainties in the experimental parameters of seed-Stokes and pump-pulse train intensity and phase.

## II. Second Stokes Generation

As a final topic in the discussion of transient stimulated Raman amplification, we will discuss the results of experiments that studied the generation of second-Stokes radiation. This is an important subject since it is the appearance of higher-order Stokes light that not only makes for a much more complicated Raman interaction, but also usually signals the end of a purely Raman process and the start of an uncontrolled, four-wave-mixing dominated regime.<sup>8-16</sup> When that



happens, self-similar solutions are no longer applicable to the interaction and the effects of phonon-field phase memory are lost in other processes. As we will see below, the generation of higher-order Stokes wavelengths and the subsequent introduction of four-wave mixing is extremely hard to avoid in any real system.

There are basically two ways that a Raman system can be driven to produce light at the second-Stokes frequency. One way is for the Stokes signal to grow so strong that it acts as a pump frequency in its own right, and therefore produce a signal shifted by another Stokes frequency. This process could continue, if the gain in the material system were high enough, so that many orders of Stokes are created. This concept is illustrated in Fig. 4. For this idealized representation, each Stokes order is shown to give rise to the next Stokes order and each successive pump is depleted completely. The gradual decrease in overall intensity from one order to the next is simply a consequence of the difference in photon energies between each successive pump and Stokes wavelength.

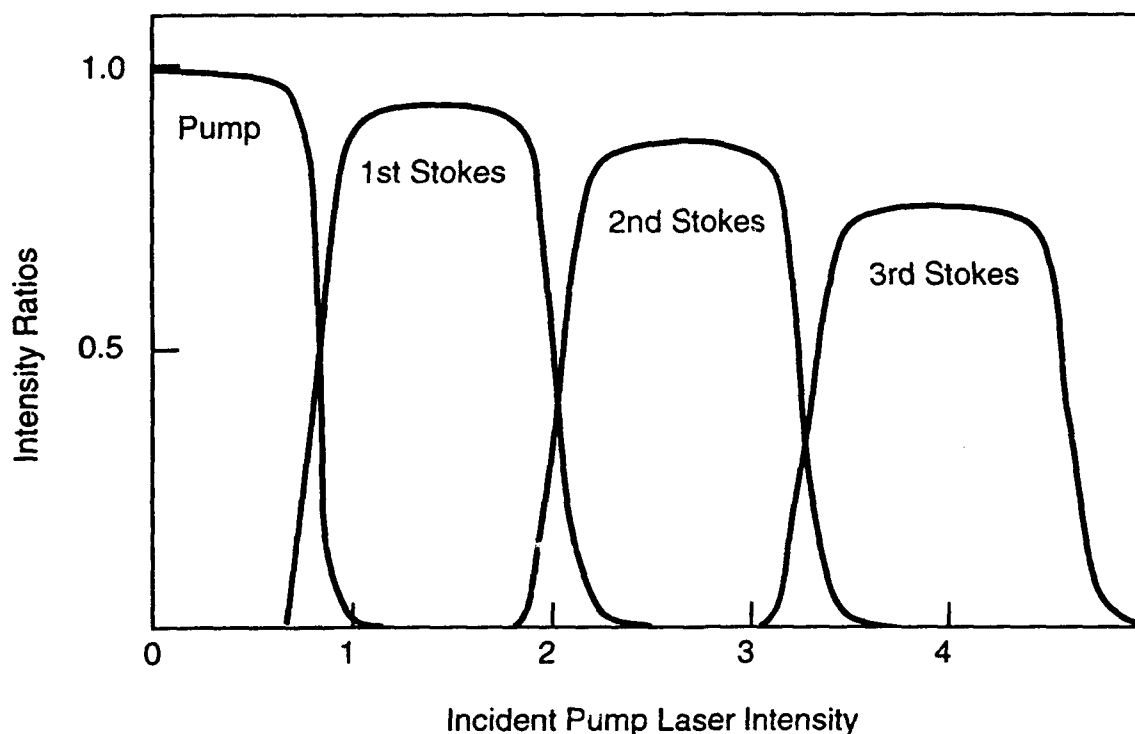


Figure 4. Schematic representation of a cascade process in which multiple orders of Stokes light are generated.

The other method by which second Stokes can be created is through a four-wave-mixing process in the Raman medium.<sup>8-12</sup> This nonlinear process is caused by the presence of high intensity fields at both the pump and first-Stokes frequencies and is dependent on the Raman resonance condition in the material, but is different from stimulated Raman growth in that there is no

transfer of energy to the medium and the process must be phase matched to be able to grow. For almost all gases, this phase-matching condition can be satisfied when the Stokes field is at a very small angle away from the propagation axis of the pump beam. This angle depends on dispersion in the medium and therefore on gas pressure and on the magnitude of the Stokes shift. At moderate gas pressures, the phase-matching angle will be small and the four-wave-mixing radiation will be generated within the angular spread of the Stokes beam. In this case the four-wave-mixing radiation at the second-Stokes frequency becomes a seed for the stimulated Raman amplification at the second-Stokes frequency. The phase-matching angle is large compared to the beam spread angle only for high pressures in gases such as  $H_2$  and  $D_2$ , which have large Stokes frequency shifts.

In an effort to separate the effects of four-wave mixing and stimulated Raman scattering, we performed an experiment that used a single Raman cell filled with deuterium gas at pressures of 15 to 140 atm.<sup>16</sup> The production of first- and second-Stokes light was monitored as a function of 532 nm pump energy. Because of the small angles involved, we did not attempt to physically separate the second-Stokes signal that was generated by the stimulated-Raman process from the second-Stokes signal that was generated by four-wave mixing. Instead, we monitored the total energy at both the first- and second-Stokes frequencies and plotted those signals as a function of 532 nm pump energy. The results are shown in Fig. 5. At each pressure the first-Stokes energy rises steeply before reaching a plateau at the onset of pump depletion. Since it is the logarithm of the ratio of each Stokes energy to the 532 nm pump energy that is displayed in Fig. 5, a plateau corresponds to a linear dependence of the Stokes energy on the pump energy. The second Stokes appears at a low energy level almost immediately after the first-Stokes energy becomes significant. Immediately after an initial fast rise, the second-Stokes pulse energy enters a region in which it increases slowly, or not at all, depending on the pressure, as the 532 nm pump energy increases. At still higher 532 nm pump energies, a pressure-dependent, threshold-like behavior is observed for the second-Stokes energy, characterized by the onset of rapid growth. This region is followed by a plateau in the second-Stokes energy at the highest pressures which we associate with the onset of first Stokes depletion. Similar trends were observed when using hydrogen instead of deuterium.

We interpret the data from Fig. 5 to indicate that second-Stokes generation from four-wave-mixing processes is always present when stimulated Raman processes occur. In the case of high pressure in deuterium, the presence of the second-Stokes signal generated from four-wave mixing is indicated by the initial plateau region in the second-Stokes signal. That signal stays five orders of magnitude smaller than the first-Stokes signal and does not seem to affect the threshold point for the growth of the second-Stokes signal generated from the stimulated Raman process. It is not growing exponentially, but instead is proportional to a product of the pump and first-Stokes fields, as would be expected for a four-wave-mixing process. The signal level is small because the phase matching is poor on-axis and very little growth can occur in the four-wave-mixing signal.

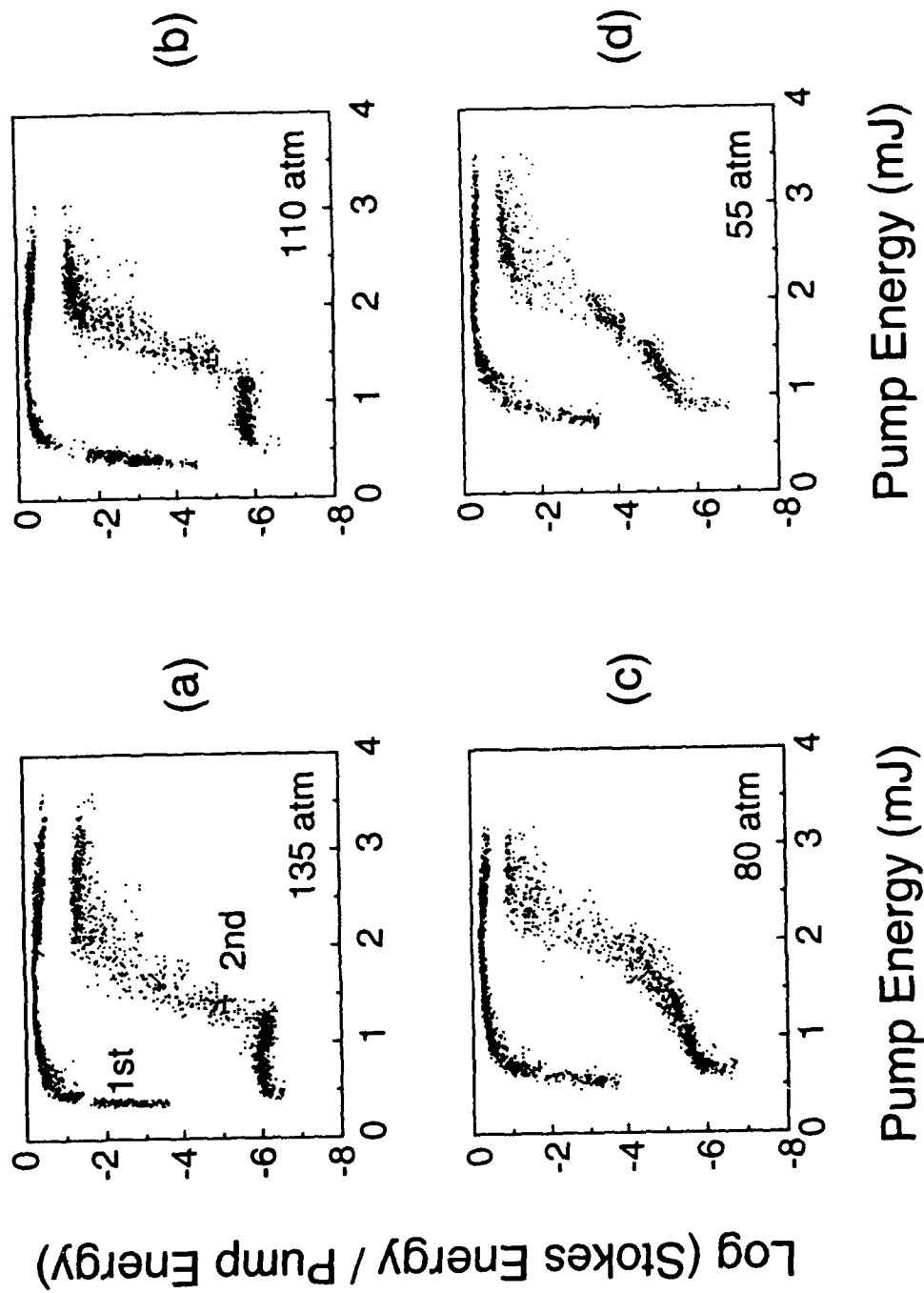


Figure 5. First and second Stokes generation in deuterium at four different pressures as a function of the 532 nm pump energy (a) deuterium pressure of 135 atm, (b) 110 atm, (c) 80 atm and (d) 55 atm.

For lower pressures, however, there is no plateau region in the second-Stokes signal. This and other data indicate that the second-Stokes signal from four-wave mixing lowers the pump energy at which the total second-Stokes signal grows to be large. This is consistent with the increased amount of four-wave-mixing second-Stokes light that is generated on-axis due to the smaller phase-matching angle at lower pressures.

The amount of second-Stokes light that is generated on-axis for these examples of moderate and high pressure D<sub>2</sub> gas is less than would be encountered using almost any other gas at equivalent or lower pressure. In those cases the production of second-Stokes light will take place well before the energy of the first-Stokes reaches a level that is sufficient to generate second-Stokes light from stimulated processes. The practical consequence of this is that second- and higher-order Stokes processes will produce significant signal from almost any Raman interaction that is driven by pump energies that are more than approximately two times above the first-Stokes threshold. This makes designing experiments to study self-similar effects in stimulated Raman scattering difficult, since pump energies many times above threshold must be used. A potential solution to this problem would be to use a multi-pass cell for the Raman interaction with mirrors that only reflect the pump and first-Stokes signals. If the second-Stokes light were constantly rejected by such a system, it might be possible to drive the Raman interaction many times above threshold without generating any higher-order Stokes signals.

### III. Imaging through a low light level Raman amplifier

#### INTRODUCTION

Stimulated Raman scattering has potential to provide high gain amplification of optical signals at a noise level limited only by fundamental quantum fluctuations.<sup>17-19</sup> For example, stimulated Raman amplification can provide gains in excess of  $10^{10}$  with theoretical front end noise levels of one photon per spatial-temporal mode. A thorough understanding of the competition between the input-Stokes signal and the quantum noise in stimulated Raman amplifiers is important for optimizing their use in real optical systems. This includes understanding the scaling of the spatial modes used by both the noise signal and the input-Stokes signal in the presence of substantial spatial gain-narrowing due to high Raman gains. We have previously reported measurements of minimum input-Stokes levels needed to overcome noise in a Raman amplifier in the transient regime using 30 psec duration pulses.<sup>20</sup> Here we report results using pulses with 5 - 10 nsec duration in a system with approximately one temporal mode. We present measurements of the amplification of Stokes beams and the imaging characteristics of a Raman amplifier when the input-Stokes beam carries structure. The number of spatial resolution elements sustained by the amplifier is determined by the Fresnel

number as well as by the imaging geometry. Due to the limited amplifier pump Fresnel number of approximately 17 currently available in this experiment, we expected resolution to be limited. We used two different strategies to preserve image characteristics. In one, the image was amplified directly, while in the other, the Fourier transform of the image was amplified. When the amplifier is short compared to the diffraction length of the structure, corresponding to large Fresnel numbers, amplification of the real image can sacrifice field of view due to spatial gain-narrowing, while amplification of the Fourier transform can sacrifice edge definition while retaining maximum field of view. At smaller Fresnel numbers, when the length of the amplifier is comparable to the diffraction length of the structure of the image, both techniques are likely to provide limitations on both field of view and edge definition. In the course of presenting our measurements we make comparisons of the image quality for these two imaging techniques. In each case we determine the minimum input Stokes level needed to compete with the quantum noise generated signal to give a signal-to-noise (S/N) ratio of 1 in the output signal. For all situations the input signal needed to provide a signal-to-noise ratio near unity was only a few photons per spatial-temporal mode, approaching fundamental quantum noise limitations. In addition, at the lowest signal levels, we show that the input-Stokes field interferes with the field amplitude of the zero point vacuum fluctuations to produce intensity modulations in the amplified signal.

#### APPARATUS

The apparatus used for our experiments is shown in Fig. 6. A 10 nsec pulse with an energy of approximately 120 mJ at 1.06  $\mu\text{m}$  was produced by an injection-seeded Nd:YAG oscillator. The beam was spatially filtered with a vacuum pinhole and then recollimated. It was subsequently expanded in a telescope so that the diameter of the first minimum of the Airy pattern matched that of the 9 mm Nd:YAG amplifier rod. The resulting beam was apertured at the first Airy minimum and amplified. The amplified beam had a smooth profile and about 300 mJ of energy at 1.06  $\mu\text{m}$ . This beam was then converted to the second harmonic with a doubling efficiency of 26%, producing about 78 mJ at 532 nm. The laser oscillator was fully locked to a single longitudinal mode more than 99% of the time, and the energy in the second harmonic pulses fluctuated by no more than  $\pm 5\%$ .

Twenty four per cent of the available second harmonic pump light was separated with a beam splitter to produce the seed-Stokes beam. In order to obtain seed-Stokes signals that were smooth in time we found it necessary to use a combination of a self-generator and a preamplifier. The 1-m self-generator cell was operated below pump saturation at a pressure of 20 atmospheres, chosen so that the spectral width of the gain-narrowed Raman line approximately matched the spectral width of the pump pulse. Under these conditions the light from the self-generator was produced in the second half of the pump pulse with a sharp leading spike and a smooth tail. The seed pulse was preamplified using a pump beam that was delayed by 5 nsec in order to amplify just the smooth later part of the

seed-Stokes pulse. Approximately 12% of the original second harmonic energy or 9 mJ was used to pump the 1 m preamplifier, driving it to saturation. The resulting Stokes signal pulse had a duration of the order of 4-5 nsec and an energy of about 1 mJ.

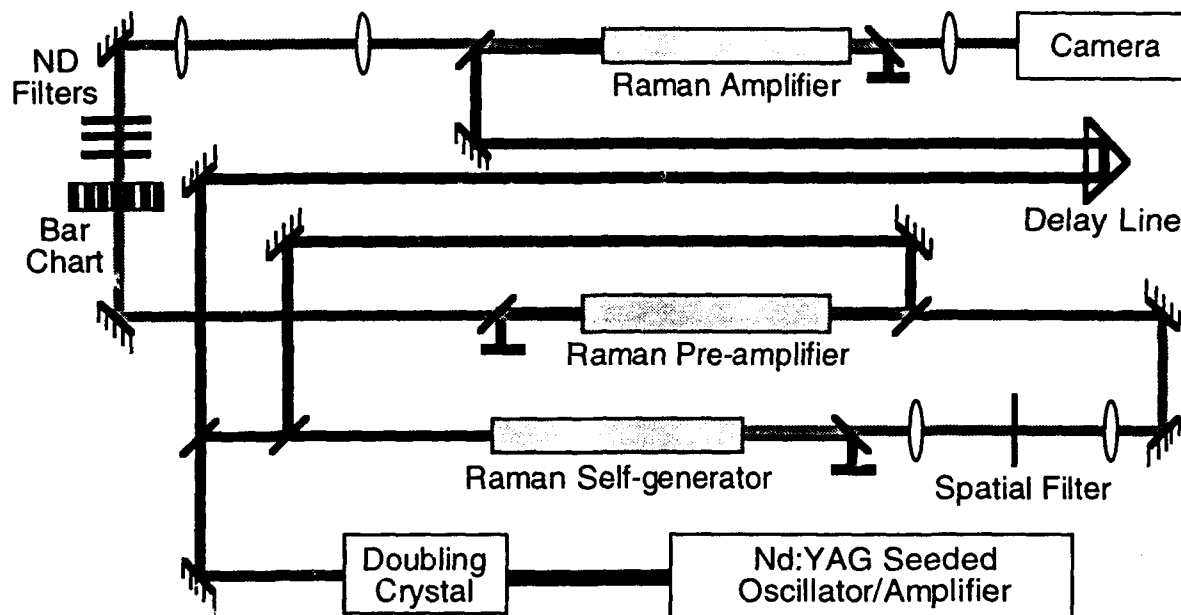


Figure 6. Schematic of the experimental apparatus.

The output of the Stokes preamplifier was spatially filtered and then collimated at a diameter of 5.2 mm, corresponding to a Fresnel number of 31 for our 1-m amplifier cell. The seed-Stokes signal was brought into the 1-m long amplifier cell, which was held at the same pressure as the seed-Stokes generator and preamplifier cells. The pump and Stokes beams were combined before the amplifier with a dichroic mirror, and propagated collinearly through the amplifier.

In order to impose structure on the input-Stokes signal a resolution bar chart was placed in the beam. The width of the bright and dark bars in the resolution chart was chosen to be 0.315 mm, giving a spatial period of 0.63 mm, in order to ensure that the seed-Stokes beam would not diffract out of the gain column significantly. In addition, the total illuminated area of the resolution bar chart was restricted to about 1 mm, enabling a uniform illumination with the central portion of the 5.2 mm diameter seed-Stokes beam. With the bar chart in use, either its real image or the image of its Fourier transform was relayed into the Raman amplifier. For the various measurements the position of the image of the bar chart or of its Fourier transform was placed at the entrance, middle or exit of the amplifier by moving the amplifier cell. The size of the real image or the image of the Fourier transform

was then adjusted to match the size of the pump beam in the Raman amplifier. In these measurements, the energy of the full seed-Stokes beam transmitted by the bar chart was about  $5 \mu\text{J}$ . The seed Stokes was attenuated by neutral density filters of ND 9 to ND 12 before the bar chart to obtain a low-light-level signal beam. As the seed-Stokes level was changed the neutral density filters at the camera had to be adjusted accordingly to keep the camera response in range.

After the amplifier cell the amplified-Stokes beam was separated from the transmitted pump with dichroic mirrors and spectrally selective filters. It was imaged on an intensified CCD camera, and the resulting data was stored digitally. Two techniques depicted in Fig. 7 were used to form the image of the amplified beam at the camera depending on the configuration used for bringing the seed-Stokes beam into the amplifier. When a real image of the bar chart in the amplifier cell was used, a simple lens placed after the amplifier imaged the first image plane of the bar chart onto the camera. When the image of the Fourier transform of the bar chart was used, a lens placed after the amplifier produced the Fourier transform of the transform plane at the camera, reconstructing an image of the original chart.

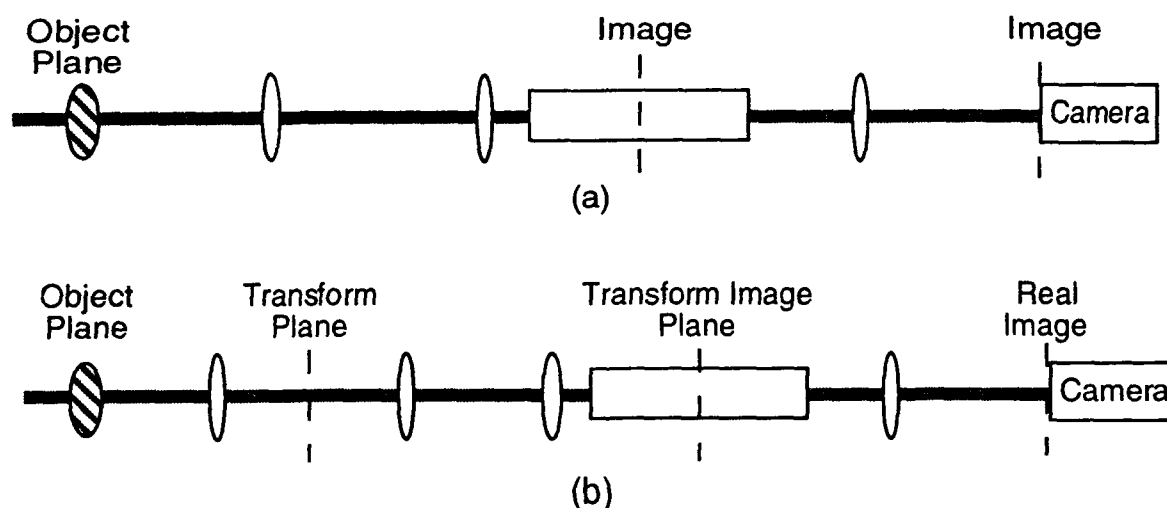


Figure 7. A schematic of the experimental configurations used for imaging into a stimulated Raman amplifier. (a) The object plane is imaged directly into the amplifier using a telescope, and then reimaged onto the camera plane using a simple lens. (b) The spatial Fourier transform of the object plane is produced by a simple lens and the Fourier transform plane is imaged into the amplifier using a telescope. The Fourier transform plane is then retransformed by a simple lens to give a real spatial image at the camera plane.

## EXPERIMENTAL RESULTS

In Figs. 8,9 we show a series of results for the low-light-level image amplification of a resolution bar chart. Figure 8 shows our experimental results when a direct image of the bar chart was amplified in the Raman amplifier cell. The bar chart was imaged into the center of the Raman amplifier cell for the data presented in Fig. 8, but the results were similar when the image was placed at the entrance plane or the exit plane of the amplifier. Figure 8(a) is an image of the signal produced by amplified quantum noise from the Raman amplifier cell with no input Stokes present. The gain in the amplifier was approximately  $1.4 \times 10^4$ . The signal in this case is random in nature and produces a changing spatial pattern from shot-to-shot. Figure 8(b) shows an image of the resolution bar chart illuminated by the input-Stokes beam but with no gain in the amplifier. In this case, the diameter of the illuminated region of the resolution bar chart is 0.135 cm and is well contained in the 0.34 cm diameter of the pump beam. Figure 8(c) shows the amplified signal with the same gain as in Fig. 8(a), but with approximately 210 input-Stokes photons in the incident image. A bar pattern is detectable, but the noise is still quite evident. Figure 8(d) shows an image produced using 800 input-Stokes photons and shows moderate noise with a relative camera sensitivity which is 0.3 times that under which the images in Figs. 8(a) and 8(c) were taken. As more input-Stokes photons were used, images with better signal-to-noise ratios were produced as shown in Figs. 8(e) and 8(f) with  $3.2 \times 10^4$  and  $1.5 \times 10^{10}$  input-Stokes photons, respectively.

Figure 9 presents results obtained by imaging the Fourier transform of the resolution bar chart into the Raman amplifier cell, and then retransforming the image at the camera plane. For these results the Fourier transform plane was located at the exit window of the Raman amplifier, although very similar results were recorded at other locations along the cell axis. In this case the size of the Fourier transform was approximately matched to the amplifier in that the Rayleigh range of the largest structure in the transform (determined by the width of the bright bars) was made equal to the length of the amplifier, and the Rayleigh range of the smallest structure (determined by the illuminated region of the bar chart) was adjusted so it would increase in size to match the large structure over the amplifier length. In this manner it was estimated that most of the photons passing through the bar chart would be effectively amplified, and would provide a reasonable measure of the minimum signal level needed to overcome noise. Figure 9(a) shows the amplified-Stokes signal originating from quantum noise when the cell is pumped to give a Raman gain of  $4 \times 10^4$ . The spatial pattern of the output Stokes generated from noise varied from shot-to-shot and had a characteristic structure size that was related to the Fourier transform of the noise as presented in Fig. 8(a). Figure 9(b) shows an image of the resolution bar chart reconstructed using only the input-Stokes light with no amplification. Figure 9(c) is a reconstructed image for an illumination level of 40 Stokes photons at the bar chart and with the same gain in the amplifier as for Fig. 9(a). The vertical bars are able to be identified even though the structure size of the noise is very apparent. Figure 9(d) shows the output signal with 450 input-Stokes

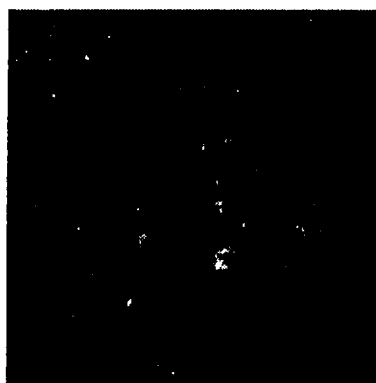




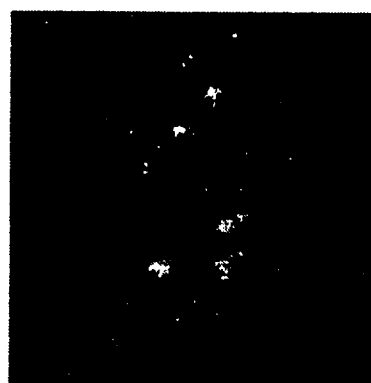
(a)



(b)



(c)



(d)



(e)



(f)

Figure 8. Bar chart is illuminated by the seed-Stokes beam and the image is relayed with unity magnification to the center of the Raman amplifier cell. The plane at  $z=50$  cm is imaged using a 50 cm focal length lens onto the camera. (a) Noise, sensitivity=1; (b) seed Stokes alone; (c)  $\sim 210$  seed-Stokes photons; sensitivity=1; (d)  $\sim 800$  seed-Stokes photons; sensitivity=0.3; (e)  $\sim 3.2 \times 10^4$  seed-Stokes photons; sensitivity =  $7.4 \times 10^{-3}$ ; (f)  $\sim 1.5 \times 10^{10}$  seed-Stokes photons; sensitivity =  $3.2 \times 10^{-8}$ , Gain  $\sim 1.4 \times 10^4$ .

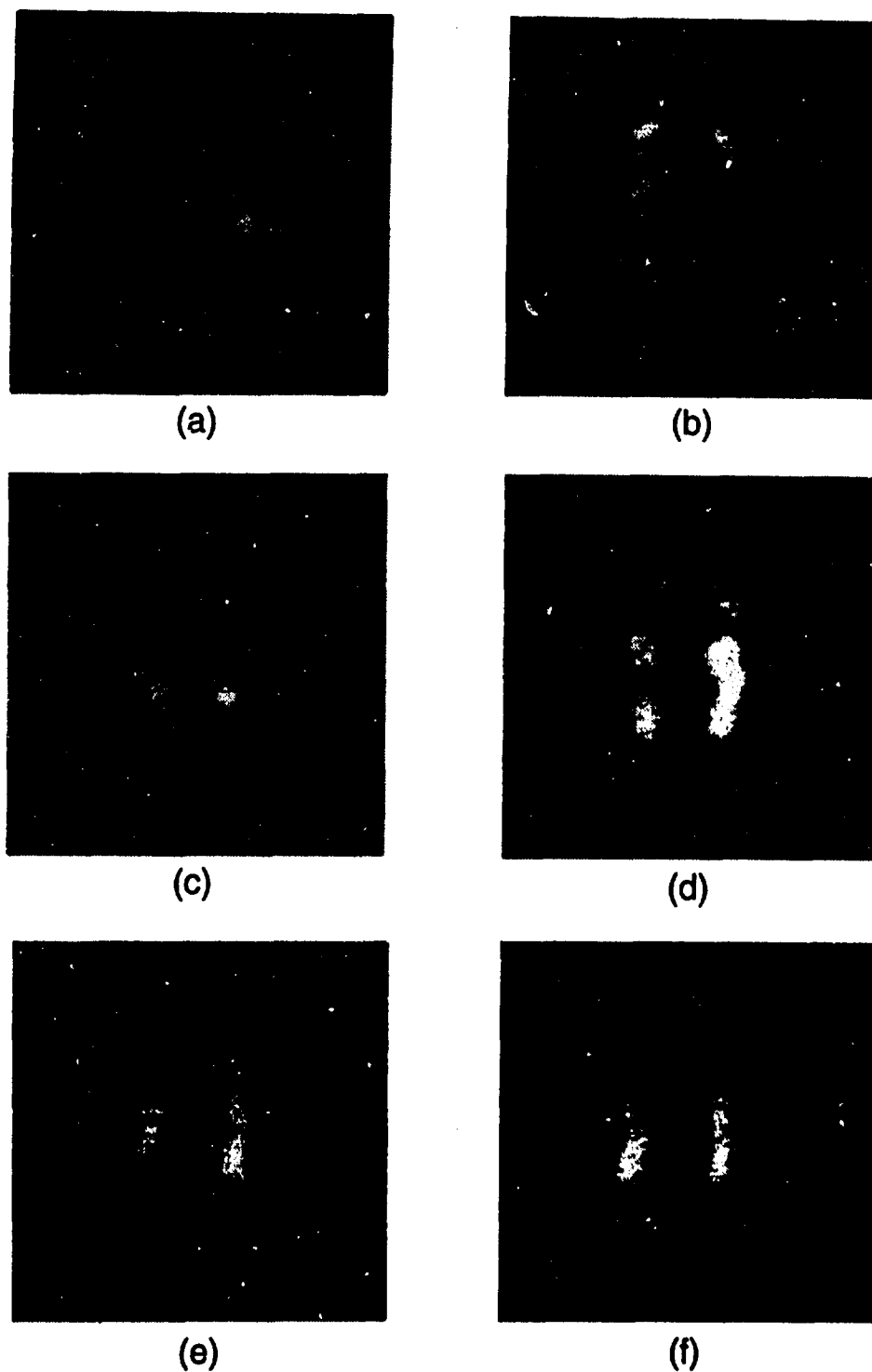


Figure 9. Fourier transform of bar chart illuminated by seed-Stokes beam is placed at the exit window of the Raman amplifier cell. The plane at  $z=100$  cm is Fourier transformed reproducing an image at the camera. (a) Noise, sensitivity = 1; (b) seed Stokes alone - no amplification; (c)  $\sim 40$  seed-Stokes photons; sensitivity = 1; (d)  $\sim 450$  seed-Stokes photons; sensitivity = 0.25; (e)  $\sim 9.9 \times 10^4$  seed-Stokes photons; sensitivity =  $9.3 \times 10^{-4}$ ; (f)  $\sim 9.5 \times 10^8$  seed-Stokes photons; sensitivity =  $1.8 \times 10^{-7}$ . Gain  $\sim 4 \times 10^4$

photons and a camera sensitivity of 0.25 relative to Figs. 9(a) and 9(c). The overall noise level is reduced due to the changed camera sensitivity, but the vertical signal bars are still strongly modulated by the interference of the signal field with the quantum noise field. Figures 9(e) and (f) show increased smoothness in the vertical signal bars with  $10^5$  input-Stokes photons and  $10^9$  input-Stokes photons at camera sensitivities of  $10^{-3}$  and  $10^{-7}$ , respectively.

## DISCUSSION

In order to make a meaningful comparison of the noise characteristics of our Raman amplifier in the two different imaging configurations, and to make a comparison with fundamental quantum noise considerations, it is necessary to determine the number of spatial-temporal modes that are effective in our amplifier. The average quantum noise level is one photon per spatial-temporal mode although, on a given laser shot, statistical fluctuations of 100% or more are possible. We have independently determined that at our gains of  $10^4$ - $10^5$  there are 1.8 temporal modes in our amplifier. The determination of the number of spatial modes that are effective in our Raman amplifier is somewhat more difficult. The number of spatial modes of a single polarization  $N_{\perp}$  in a long, narrow, uniform gain column of cross-sectional area  $A$  and length  $L$  has been discussed elsewhere,<sup>21</sup> and shown to be given by the relation

$$N_{\perp} = A^2 / \lambda^2 L^2 = F^2 \quad (1)$$

where  $F$  is the Fresnel number. However, significant spatial gain-narrowing occurs over the length of the amplifier and the gain-narrowed, amplified signal Stokes can have a different size from the gain-narrowed, amplified noise Stokes. We have chosen to use the diameter of the gain-narrowed amplified Stokes noise to determine the effective Fresnel number for the number of noise modes since this choice satisfies the approximation of a uniform gain profile most closely.

We are now prepared to determine the illumination level needed to produce images at a signal-to-noise ratio of approximately 1 from our Raman amplifier. For the case of direct imaging into the Raman amplifier, approximately 210 photons are needed to produce an image with a S/N of approximately 2, for the data shown in Fig. 8(c). The Fresnel number of the gain-narrowed noise for that configuration is  $\sim 4.3$ , corresponding to a total of 18.5 spatial modes. When combined with the 1.8 temporal modes, this data indicates that 3 input-Stokes photons per mode are needed to give a S/N of 1 after an amplification of  $10^4$ . This is comparable with the expected quantum noise level of 1 photon per mode. The remaining difference could be due to non-optimal matching of the beam sizes.

We can analyze our Fourier transform results using the same type of reasoning as above. Using the same gain-narrowed noise size, since the gain is the same as for the data in Fig. 8, we see from Fig. 9(c) that 40 input-Stokes photons are needed to produce a S/N of approximately 1. In this case, however, the Fourier transform reconstructs an image of the bar chart, but produces a Fourier

transform of the noise from the amplifier cell. Because of the size we chose for the Fourier transform in the Raman amplifier cell, the retransform of the image at the camera is smaller than the transformed noise. In essence, we have provided a spatial filter for our process and we need to take account of the reduced number of noise modes by observing the overlap of the signal with the transformed noise. We thus find that instead of having  $\sim 18.5$  effective spatial modes, there are approximately 12 effective spatial modes for the data in Fig. 9(c). Thus, for the case of a Fourier transformed image in the amplifier we deduce that  $\sim 2$  input-Stokes photons are needed to provide a S/N of 1 in the output signal. The lower signal level needed with the amplification of the Fourier transform as compared with that needed with direct image amplification to produce a S/N  $\sim 1$  may be due to the improvement provided by the effective spatial filter in the image reconstruction process.

A comment should be made on the difference that our two different imaging techniques give in resolution and field of view. A comparison between Fig. 8(f) and Fig. 9(f) shows a small but definite decrease in resolution for the Fourier-transformed image of Fig. 9(f). This is to be expected since the higher spatial frequencies were lost due to the limited size of our pump beam and due to our choice of Fourier-transformed image size in the amplifier cell. What is not seen, due to the small field of view produced from our apertured resolution bar chart, is an increased field of view in Fig. 9(f) over that of Fig. 8(f). This effect is expected since the Fourier transform automatically preserves the large structure of the object, and has been confirmed in other results not presented here. We thus conclude that the choice of an imaging technique can be determined by whether the field-of-view or the image resolution is the most important parameter in an imaging application.

At the lowest seeding levels intensity modulation is visible along the bright bars of the amplified image of the resolution bar chart. This modulation is most easily seen in the Fourier transform images shown in Fig. 9. We observed strong modulation along the bar images for input seed-Stokes beams having up to  $\sim 500$  photons, and less modulation as the level approaches 1000 photons. For higher seed-Stokes levels the bar images became uniform in intensity.

### Competition between signal and noise in narrowband Raman amplifiers

There is both theoretical and practical interest in understanding the competition between noise and signal in a Raman amplifier. We have previously studied the effect of spatial and temporal noise on the amplification of low-level input Stokes signals in transient Raman amplifiers with pump linewidths comparable to, or wider than, the gain-narrowed Raman linewidth.<sup>19</sup> Those studies have verified that noise levels exist at a level of one photon per spatial-temporal mode in the vacuum noise field and images with signal-to-noise ratios of unity have been obtained with real input signals near one photon per spatial-temporal mode of the amplifier.

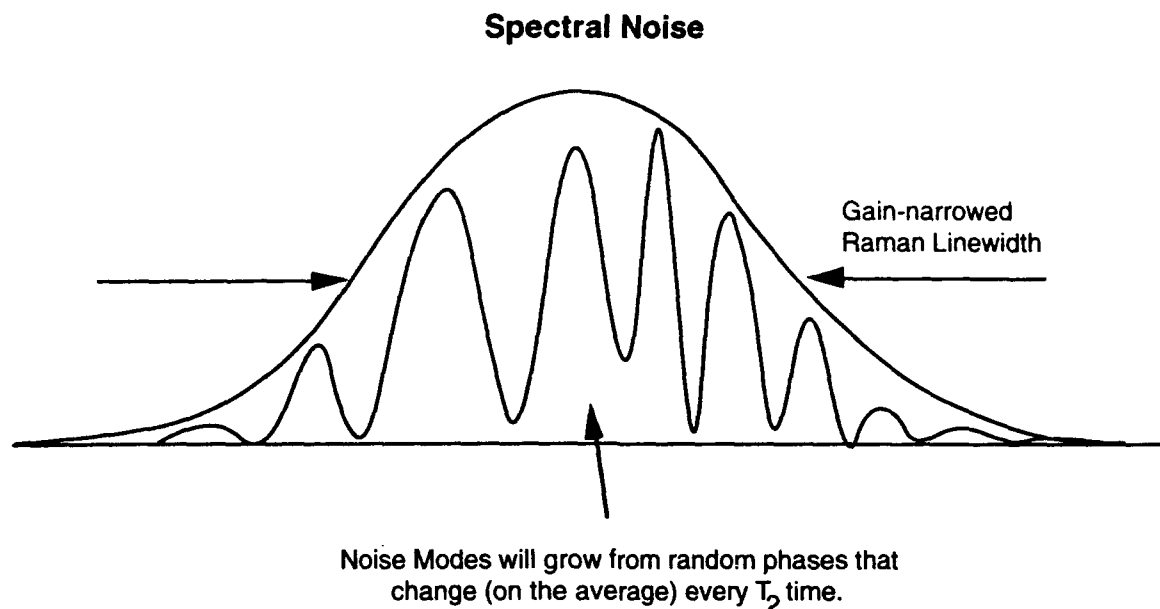


Figure 10. Schematic showing noise modes within the gain narrowed Raman linewidth

We also considered the competition between signal and noise in a Raman amplifier in which both the pump and Stokes linewidths were narrow compared to the Raman linewidth. For a Raman self generator operated under these conditions, it has been shown that the amplified Stokes noise varies randomly in linewidth from a minimum of the pump linewidth to a maximum of several times the gain-narrowed Raman linewidth.<sup>22</sup> We examined the effect of noise on an amplified signal that was also narrow-band compared to the Raman linewidth. We determined the minimum signal levels necessary for the amplified Stokes signal to compete with the noise signal and, in particular, determined whether noise over the entire Raman linewidth competes with the input signal. We also determined the extent to which noise corrupts the coherence of a narrow-band input at various input Stokes signal levels. The effect of detuning the input Stokes signal more than one pump linewidth away from the Raman line center was investigated, and the temporal and spatial characteristics of the amplified Stokes pulse were studied. Both single shot and time averaged behavior were examined.

Our experimental apparatus shown in Fig. 11 consisted of a single longitudinal mode, injection locked Nd:YAG laser with a pulse length of 10 ns FWHM. The 1.06  $\mu\text{m}$  pulse was amplified to 300 mJ and doubled into the green. The energy available at 532 nm was  $\sim 150$  mJ and the pulse had a linewidth of 50 - 100 MHz, close to the transform limit. Methane and deuterium were used as Raman media and provided the experimental parameters listed below. Temporal characteristics of the signal were measured with a 2-ps resolution streak camera, and spatial characteristics were captured with a low-light-level CCD camera. The characteristics of the amplified Stokes signal were studied as the input Stokes level was reduced.

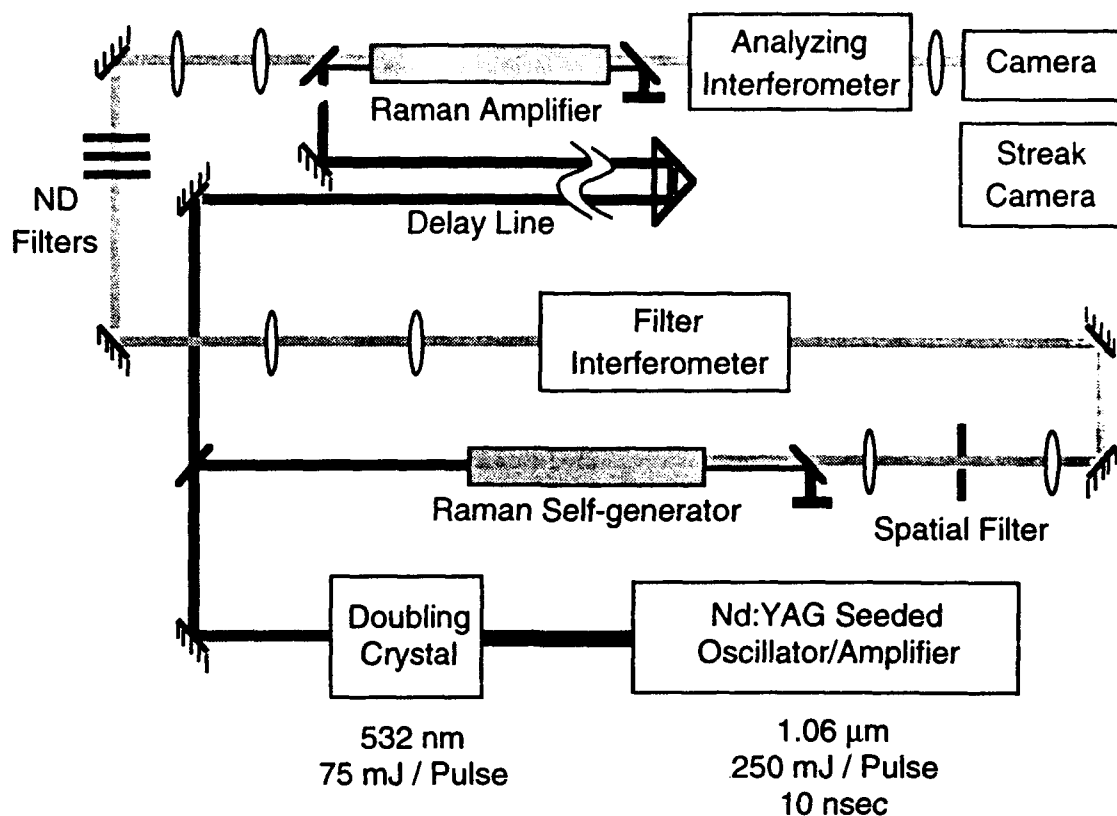


Figure 11. Schematic of experiment used in studies of spectral noise seeding.

### Experimental Parameters

Raman Medium:	D <sub>2</sub> gas at 1200 psi	CH <sub>4</sub> gas at 600 psi
Raman shifted wavelength:	632.5 nm	629.7 nm
Raman linewidth:	5.28 GHz	~20 GHz
Exp. Gain narrowed width:	1.13 MHz	5 GHz
Gain narrowing factor:	4.6	4 - 5

Stokes Filter Interferometer			Analyzing Interferometer		
	D <sub>2</sub>	CH <sub>4</sub>		D <sub>2</sub>	CH <sub>4</sub>
Length:	4.5 cm	1.0 cm	Length:	10 cm	2.0 cm
FSR:	3.3 GHz	15 GHz	FSR:	1.5 GHz	7.5 GHz
Finesse:	33	33	Finesse:	~40	~40
Resolution:	100 MHz	450 MHz	Resolution:	38 MHz	190 MHz

Table 1

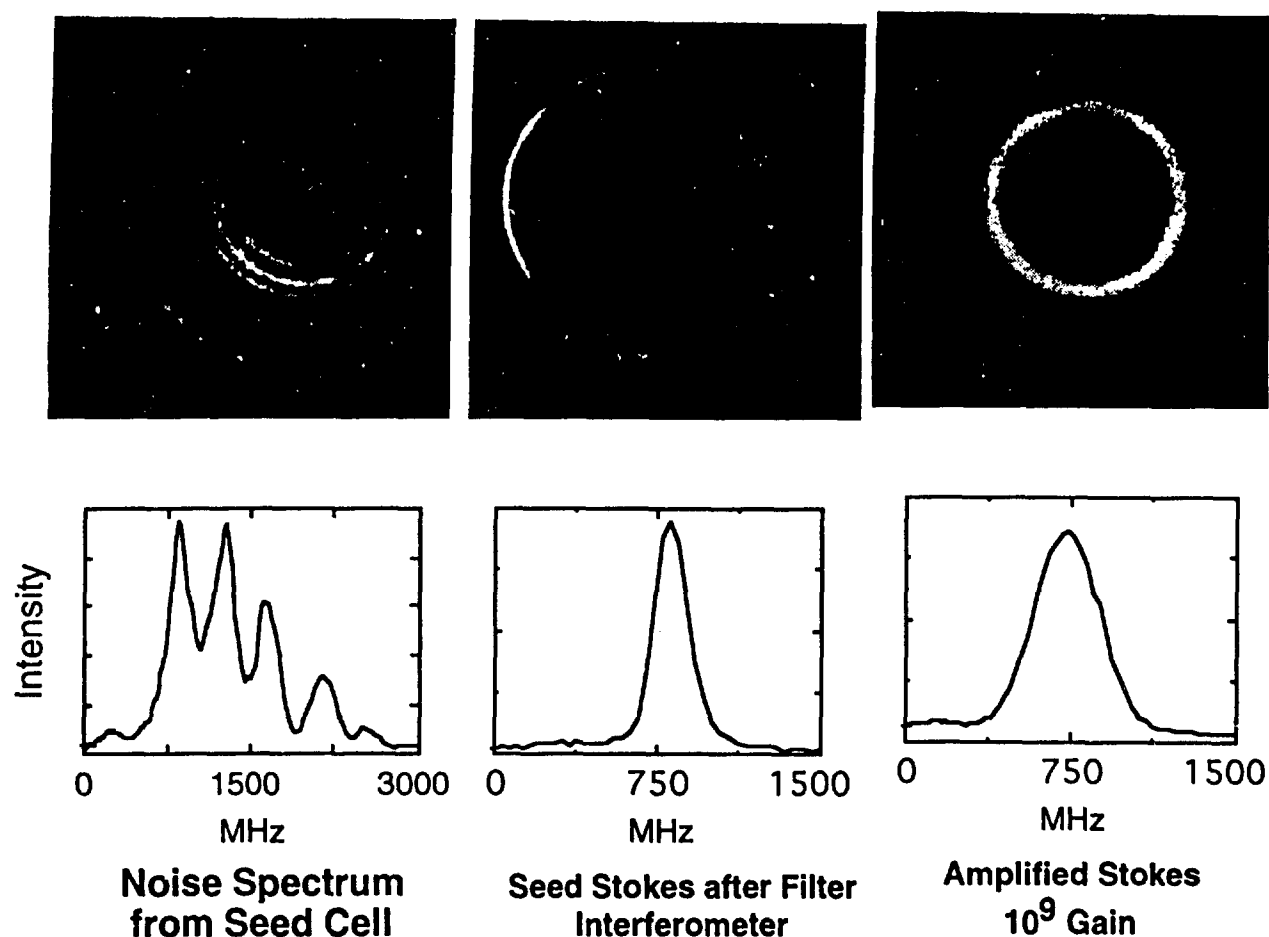


Figure 12. Typical spectra of seed Stokes and amplified Stokes obtained using deuterium.

The measurements indicated that 7 seed-Stokes photons per frequency mode were needed to compete with noise in the Raman amplifier. Problems with the current experiment were (1) a shot-to-shot intensity variation on the pump leading to both variations in the seed-Stokes level and in the level of amplification; (2) The signal was hard to distinguish from the noise and the measurement would have been improved if a spectral pattern had been imposed on the seed-Stokes signal; (3) The gain was very sensitive to the absolute frequency of the seed Stokes (if the frequency is off line center by 15% of the FWHM, the gain is expected to be down by a factor of 90 at a gain of  $e^{30}$ ).

#### Applications of Quantum limited imaging in a stimulated Raman amplifier to time-gated imaging through scattering media

Here we describe our current work in applying quantum limited Raman amplification using 30 psec pulses to image through dense scattering material. To accomplish the imaging through scattering media, an object placed immediately before the scattering sample is illuminated with a 30

psec pulse at the Stokes wavelength. The transmitted light is then imaged into the Raman amplifier cell, where it is amplified by a pump pulse of the same duration and is then re-imaged onto a detector. The leading edge of the signal transmitted by the scatterer is predominantly forward scattered or unscattered and carries the non-degraded image information. It is this early signal which is timed correctly to overlap the pump pulse and is amplified as it transits the Raman cell. The scattered light is delayed and so is discriminated against providing contrast between the forward-scattered image-bearing light and the multiply-scattered delayed light. In our time-gating experiments we used amplifiers of sufficiently large Fresnel number to retain the spatial structure of our test objects. Results were obtained from imaging a resolution bar chart through suspensions of both 0.364  $\mu\text{m}$  latex spheres and non-dairy creamer. The maximum forward attenuation of the image bearing component of the light that was transmitted through the two samples was  $e^{28}$  and  $e^{33}$ , respectively. In the case of the non-dairy creamer sample, no image was evident using ordinary, non-time-gated imaging techniques, even with long exposures on sensitive CCD cameras. However, when the Raman amplifier was used with the time-gated pulse timed to overlap with the beginning of the transmitted Stokes pulse, a clear image of the bar chart was produced. Possible applications of this technique in medical imaging will be discussed.

#### EXPERIMENTAL RESULTS FOR QUANTUM LIMITED IMAGING

In Figs. 13 and 14 we show a series of results for the low-light-level image amplification of a resolution bar chart. Figure 12 shows our experimental results when a direct image of the bar chart was amplified in the Raman amplifier cell. The bar chart was imaged into the center of the Raman amplifier cell for the data presented in Fig. 13, but the results were similar when the image was placed at the entrance plane or the exit plane of the amplifier. Figure 13(a) shows an image of the resolution bar chart illuminated by the input-Stokes beam but with no gain in the amplifier. In this case, the diameter of the illuminated region of the resolution bar chart is 0.135 cm and is well contained in the 0.34 cm diameter of the pump beam. Figure 13(b) is an image of the signal produced by amplified quantum noise from the Raman amplifier cell with no input Stokes present and is random in nature, producing a changing spatial pattern from shot-to-shot. The gain in the amplifier was approximately  $10^5$ . Figure 13(c) shows the amplified signal with the same gain as in Fig. 13(b), but with approximately 80 input-Stokes photons in the incident image. A bar pattern is detectable, but the noise is still quite evident. Figure 13(d) shows an image produced using 126 input-Stokes photons with the same conditions as in Fig. 13(c).



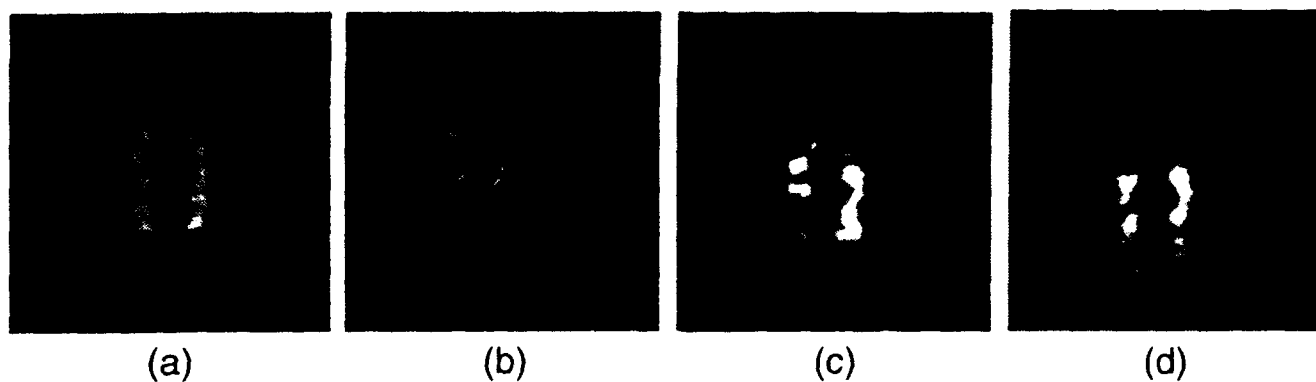


Figure 13. Images of a resolution bar chart after Stimulated Raman amplification. (a) Seed-Stokes signal, no amplification. (b) No seed-Stokes signal, gain of  $10^5$ . (c) Input of  $\sim 80$  seed-Stokes photons. (d) Input of  $\sim 126$  seed-Stokes photons.

Figure 14 presents results obtained by imaging the Fourier transform of the resolution bar chart into the Raman amplifier cell, and then re-transforming the image at the camera plane. For these results the Fourier transform plane was located at the exit window of the Raman amplifier, although very similar results were recorded at other locations along the cell axis. In this case the size of the Fourier transform was approximately matched to the amplifier in that the Rayleigh range of the largest structure in the transform (determined by the width of the bright bars) was made equal to the length of the amplifier, and the Rayleigh range of the smallest structure (determined by the illuminated region of the bar chart) was adjusted so it would increase in size to match the large structure over the amplifier length. In this manner it was estimated that most of the photons passing through the bar chart would be effectively amplified, and would provide a reasonable measure of the minimum signal level needed to overcome noise. Figure 14(a) shows an image of the resolution bar chart reconstructed using only the input-Stokes light with no amplification. With no input-Stokes signal present, Fig. 14(b) shows the amplified-Stokes signal originating from quantum noise when the cell is pumped to give a Raman gain of  $10^5$ . As in Fig. 13(b), this noise is random from shot to shot. In this case, however, it is the spatial Fourier transform of the noise as presented in Fig. 13(b). Figure 14(c) is a reconstructed image for an illumination level of 40 Stokes photons at the bar chart and with the same gain in the amplifier as for Fig. 14(a). The vertical bars are able to be identified even though the structure size of the noise is very apparent. Figure 14(d) shows the output signal with 66 input-Stokes photons and a camera sensitivity of 0.54 relative to Figs. 14(b) and 14(c).

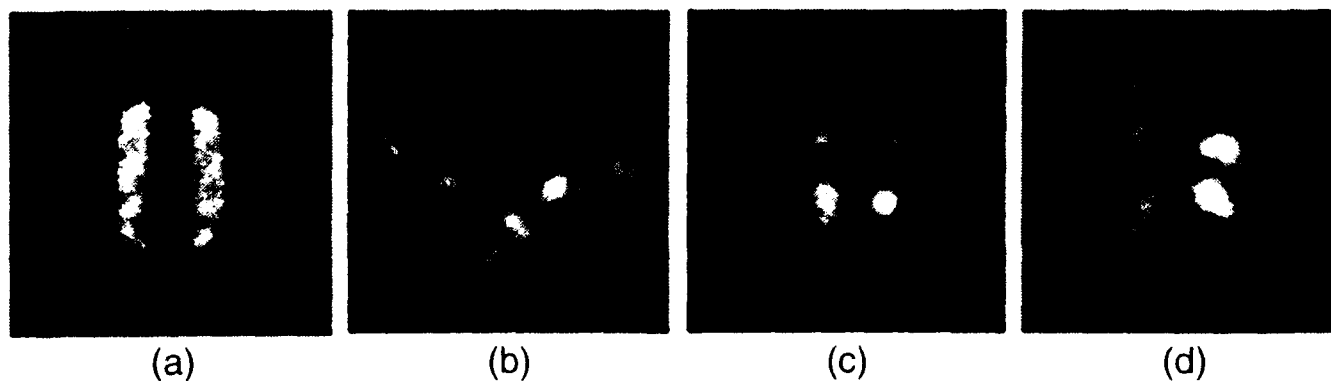


Figure 14. Images of a resolution bar chart after stimulated Raman amplification. The spatial Fourier transform of the image has been amplified. (a) Seed-Stokes signal, no amplification. (b) No seed-Stokes signal, gain of  $10^5$ . (c) Input of  $\sim 40$  seed-Stokes photons. (d) Input of  $\sim 66$  seed-Stokes photons.

#### DISCUSSION OF RESULTS FOR QUANTUM LIMITED IMAGING

We would like to compare the noise characteristics of our Raman amplifier in the two different imaging configurations with fundamental quantum noise predictions. To do this it is necessary to determine the number of spatial-temporal modes that are effective in our amplifier. The average quantum noise level is one photon per spatial-temporal mode although, on a given shot, statistical fluctuations of 100% or more are possible. We have independently determined that at our gains of  $10^4$ - $10^5$  there are 1.8 temporal modes in our amplifier. The number of spatial modes of a single polarization  $N_{\perp}$  in a long, narrow, uniform gain column of cross-sectional area  $A$  and length  $L$  has been discussed elsewhere,<sup>21</sup> and shown to be given by the relation

$$N_{\perp} = A^2/\lambda^2 L^2 = F^2 \quad (1)$$

where  $F$  is the Fresnel number. However, significant spatial gain-narrowing occurs over the length of the amplifier and the gain-narrowed, amplified Stokes signal can have a different size from the gain-narrowed, amplified Stokes noise. Because of this, we have chosen to use the diameter of the gain-narrowed amplified Stokes noise to determine the effective Fresnel number for the number of noise modes.

We are now prepared to determine the number of input photons that were needed to produce images at a signal-to-noise ratio of approximately 1 from our Raman amplifier. For the case of direct imaging into the Raman amplifier, approximately 80 photons are needed to produce an image with a

S/N of approximately 1, and 126 photons for a S/N of approximately 2 for the data shown in Fig. 13(c) and (d), respectively. The Fresnel number of the gain-narrowed noise for that configuration is  $\sim 4.3$ , corresponding to a total of 18.5 spatial modes. When combined with the 1.8 temporal modes, this data indicates that approximately 2 input-Stokes photons per mode are needed to give a S/N of 1 after an amplification of  $10^5$ . This is in relatively good agreement with the expected quantum noise level of 1 photon per mode.

We can analyze our Fourier transform results using the same analysis as above. Using the same gain-narrowed noise size as in Fig. 13, we see from Fig. 14(c) that 40 input-Stokes photons are needed to produce a S/N of approximately 1. In this case, however the Fourier transform reconstructs an image of the bar chart, but produces a Fourier transform of the noise. Because of the size we chose for the Fourier transform in the Raman amplifier cell, the re-transform of the image at the camera is smaller than the transformed noise. In essence, we have provided a spatial filter for our process and we need to take account of the reduced number of noise modes by observing the overlap of the signal with the transformed noise. We thus find that instead of having  $\sim 18.5$  effective spatial modes, there are approximately 12 effective spatial modes for the data in Fig. 14(c). Thus, for the case of the Fourier transformed image in the amplifier we deduce that  $\sim 2$  input-Stokes photons were needed to produce the image in Fig. 14(c). The S/N is clearly greater than 1 in this case but the image quality at these levels suffers from the influence of photon statistics, causing a modulation on the signal. The lower signal level needed with the amplification of the Fourier transform as compared with that needed with direct image amplification to produce a S/N  $\sim 1$  may be due to the improvement provided by the effective spatial filter in the image reconstruction process.

#### IV. Imaging through scattering media

The use of a time gate for imaging through scattering media has been demonstrated in several different systems using various methods. In these techniques the time gate is set to select light that is transmitted through the material in the least time. This light is either unscattered or dominantly forward scattered, and therefore suffers the least image degradation. Such systems have potential uses in applications such as detection of human tumors in soft tissue, and non-invasive inspection of objects in diffusive media. An ideal system for this procedure is one that has a short time gate, of the order of picoseconds or less in the case of tissue analysis. The gate should provide substantial discrimination against the time-delayed scattered light since it can contain most of the pulse energy and therefore cause noise or loss of image contrast. The gate should also be highly transmissive for the image-bearing component, and allow detection of as few photons as possible in order to minimize the sample illumination requirements and allow imaging through dense scattering samples. It is also desirable for the gate to provide two-dimensional images with a minimum of signal processing.

A number of techniques have been used to provide time-gated imaging. Electronic gating has been used to provide time resolution of  $\sim 80$  psec,<sup>23</sup> streak cameras have provided resolutions of the order of 10 psec,<sup>24,25</sup> optical Kerr gates have been used with resolution of the order of 10 psec,<sup>26,27</sup> optical coherence tomography<sup>28-30</sup>, holography with either short pulses<sup>31,32</sup> or broad-band, long-pulse radiation<sup>33</sup> has provided time resolution down to  $\sim 150$  fsec. While all of these systems have been used to produce time-gated images with subnanosecond, and some with picosecond and subpicosecond resolution, each has its own limitations. Systems based on streak cameras do not provide direct two-dimensional images, and the signal must be built up from points or scan lines. In systems based on femtosecond holography the fringe visibility can be washed out if the energy in the delayed part of the signal is too strong relative to the energy in the forward scattered component. Electronic gating has a temporal resolution that is currently limited to relatively long times. Kerr gate techniques suffer from both limited contrast capability and transmission losses.

#### APPARATUS FOR IMAGING THROUGH SCATTERING MEDIA

Using a stimulated Raman amplifier as a time gate can provide gate times down to the subpicosecond range, direct two-dimensional imaging, detection sensitivity near one photon per spatial resolution element, and a high level of discrimination against the energy in the scattered tail of the signal. An experimental schematic of such a system based on a stimulated Raman amplifier is shown in Fig. 15. The sample is illuminated with a pulse of the desired duration at the Stokes wavelength. The scattered light is then imaged into the amplifier, which is pumped by a pulse of the same duration as the Stokes pulse, and then re-imaged onto a detector. The leading edge of the signal, which is predominantly forward scattered or unscattered and carries the image information, overlaps the pump pulse and is amplified as it transits the Raman cell. The gain in the amplifier exists for approximately the duration of the pump pulse, providing the time gating. The short sample illumination pulse provides contrast between the forward-scattered image-bearing light and the multiply-scattered delayed light. Temporal resolutions can easily be of the order of 100 fsec with pulses from available lasers such as ones based on chirped pulse amplification. The self-oscillation threshold limits the gain of the amplifier to be less than or of the order of  $10^{10}$ , while quantum noise limits the sensitivity to one photon per spatial mode. If the energy in the amplified component of the signal exceeds the energy in the scattered tail, the time-gated amplification will produce a detectable image from the scattering medium. As an example, a gain of  $10^9$  allows image detection with a signal-to-noise ratio of about 10:1 if the early, image-bearing part of the signal contains as little as  $10^{-8}$  of the energy carried in the scattered tail. The number of spatial resolution elements is limited by the number of transverse modes in the amplifier, which in turn is determined by a combination of the amplifier gain and the pump pulse energy. The spatial imaging work as described above in Section 4 demonstrates that stimulated Raman amplifiers can be used to amplify images with gains of the order

of  $10^5$  and spatial resolution  $\sim 300 \mu\text{m}$  at input signal levels approaching the quantum limit of 1 photon per mode.

The laser system used in the time-gated experiments, shown in Fig. 15, has many common elements with the system shown in Fig. 6. Due to the short pulse times needed, however, a 5 Hz, mode-locked Nd:YAG laser with pulses on the order of 40 psec in length was used to produce the pump radiation for the Raman amplifier. The  $1.06 \mu\text{m}$  light was converted to its second harmonic at 532 nm and produced pulses with about 8 mJ of energy. Self-phase modulation, a potential problem due to the short duration, high intensity pulses, was minimized to ensure that the second harmonic had a smooth temporal envelope. As in Fig. 1, the Stokes illumination pulses of about  $250 \mu\text{J}$  at 683 nm were produced in a self-generator/pre-amplifier combination that consisted of two 1-m long Raman cells containing 30 atmospheres of  $\text{H}_2$ . The Stokes light illuminated a resolution chart consisting of several equally spaced bright and dark bars of  $315 \mu\text{m}$  width, and the scattering sample was placed directly after the bar chart. The light that was transmitted through the scatterer was imaged into the 1-m long Raman amplifier cell with a demagnification of 1.5:1. The amplifier was pumped with about 2.5 mJ of 532-nm pump light which had been spatially filtered and collimated at a Fresnel number of 11, giving a gain of  $10^6$  over a gain-narrowed diameter of about 1 mm. The arrival time of the pump light at the amplifier was controlled with an optical delay line. When varied, this produced a change in overlap time between the pump pulse and the scattered Stokes light pulse and allowed the amplification of different time slices of scattered Stokes light. After amplification the Stokes image in the amplifier cell was re-imaged onto either the detection array of a Photometrics CCD camera that had a noise floor of about 5 photoelectrons per pixel or the entrance slit of a 2 psec resolution streak camera.

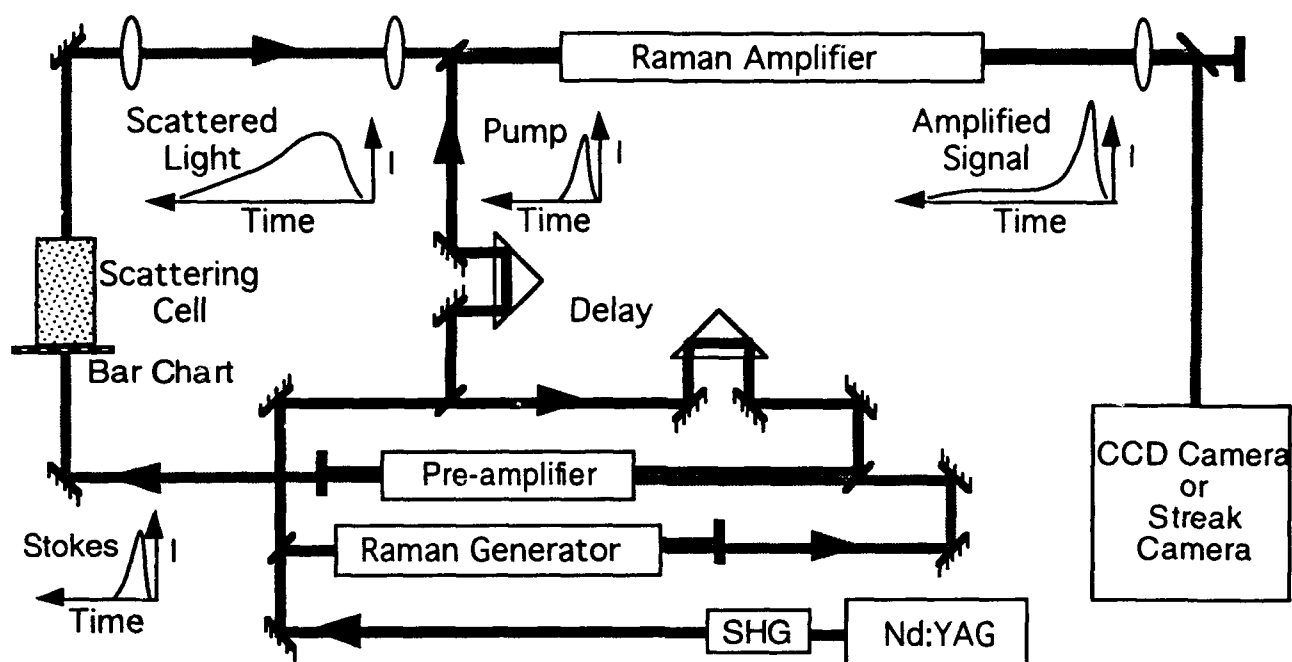


Figure 15. A schematic of the experimental apparatus used for time-gated imaging.

#### EXPERIMENTAL RESULTS FOR IMAGING THROUGH SCATTERING MEDIA

We tried several kinds of scattering media and have found different types of behavior in the various samples. One sample consisted of a 5-cm long cell containing a dense suspension of  $0.364 \mu\text{m}$  latex spheres in alcohol. In order to characterize the scattering properties of this sample we measured the total interaction coefficient  $\mu_t$  using a He-Ne laser and a  $100 \mu\text{m}$  thick sample of our suspension. The total interaction coefficient  $\mu_t$  is defined by<sup>34</sup>

$$\mu_t = \mu_a + \mu_s (1 - g), \quad (2)$$

where  $\mu_a$  is the absorption coefficient (assumed to be negligible for our samples),  $\mu_s$  is the scattering coefficient, and  $g$  is the mean cosine of the angle of scattering which gives a measure of the forward scattering produced by the sample. These measurements gave a value of  $\mu_t \approx 0.56 \text{ mm}^{-1}$ , corresponding to a decrease in direct transmission of  $e^{-\mu_t L} \approx e^{-28}$  for our 5-cm long sample. Another sample consisted of a suspension of non-dairy creamer in water at a concentration of  $5.2 \text{ mg ml}^{-1}$ . Inspection under a microscope showed the scattering particles to be generally larger than  $1 \mu\text{m}$ . Measurements of the total scattering of the non-dairy creamer in a  $100 \mu\text{m}$  long sample gave a value of  $\mu_t \approx 0.66 \text{ mm}^{-1}$ , corresponding to a decrease in direct transmission of  $e^{-\mu_t L} \approx e^{-33}$  for our 5 cm long sample.

For comparison with the time-gated images to be presented, conventional images of the bar chart and scattering cell were obtained by using the Stokes laser simply as an illuminator. The imaging geometry was identical to that used for the time-gated imaging and 100 laser shots were integrated on the CCD camera without amplification. Using the  $0.364\text{ }\mu\text{m}$  latex spheres at a concentration of  $\mu_t \approx 0.52\text{ mm}^{-1}$ , a detectable image of the bar chart was obtained, as shown in Fig. 16(a). An estimate of the contrast produced in this way can be obtained by adding the intensities of all the pixels in any one column over the region of interest and then plotting the total intensity against position. For Fig. 16(a), using the image area between the dashed lines, this gives a contrast (ratio of peak to depth) of about 1.5:1, as shown in Fig. 16(b). A similar image obtained without the scatterer in place gave an image of the bars with a contrast ratio of greater than 500:1. For these images apertures were used in the beam train to restrict the acceptance angle to a value comparable to that of the Raman amplifier. Conventional images of the bar chart and scattering cell were also obtained when a suspension of non-dairy creamer was used. For a concentration of  $\mu_t \sim 0.66\text{ mm}^{-1}$  and 1500 laser shots, no image of the bar chart was detectable above the noise.

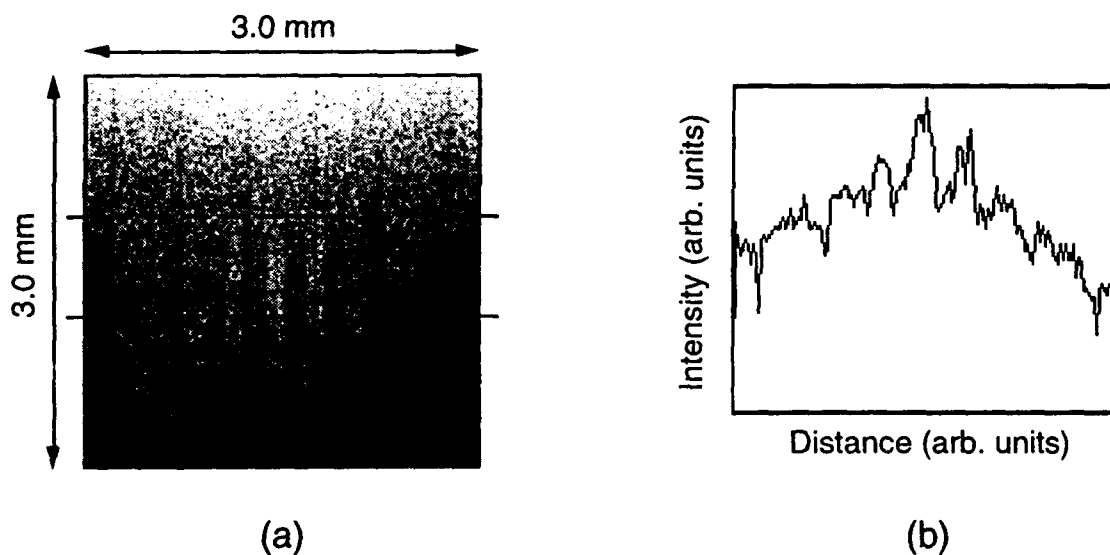


Figure 16. (a) Conventional CCD camera image produced when a bar chart was placed behind a 5 cm long cell containing  $0.364\text{ }\mu\text{m}$  diameter latex spheres in a suspension of ethanol and illuminated by  $250\text{ }\mu\text{J}$  Stokes pulses. The CCD image was the result of a 20 sec (100 laser pulses) integration on the camera. (b) A plot of integrated vertical intensity versus horizontal distance across the CCD image in (a). The integrated region is indicated by the dashed lines in (a).

Streak camera measurements were made with both the unscattered and scattered Stokes light to obtain additional information about the temporal characteristics of the scattering. A streak camera

picture taken of the bar chart without the scatterer in place is shown in Fig. 17(a). The center of the bar chart was imaged onto the streak camera slit and a time resolved image of the Stokes pulse, with the bar structure superimposed, is clearly seen. When the scattering sample of latex spheres at a concentration of  $\mu_t \approx 0.52 \text{ mm}^{-1}$  was placed after the bar chart, the scattered light generated a signal with a duration approaching 500 psec, as shown in Fig. 17(b). There was no evidence of an image of the bars in any time slice through the scattered signal within the 2 psec resolution of the streak camera. Again, apertures were used to restrict the acceptance angle to values comparable to those of the Raman amplifier. When the concentration of spheres was reduced from that used for the image shown in Fig. 17(b) to give a value of  $\mu_t = 0.41 \text{ mm}^{-1}$ , corresponding to an increase in transmission of 240, the streak camera showed a combination of a forward-scattered component containing the image, which lasted for about the duration of the Stokes pulse, and a delayed component in which no image was present. Streak camera measurements using suspensions of non-dairy creamer showed similar behavior.

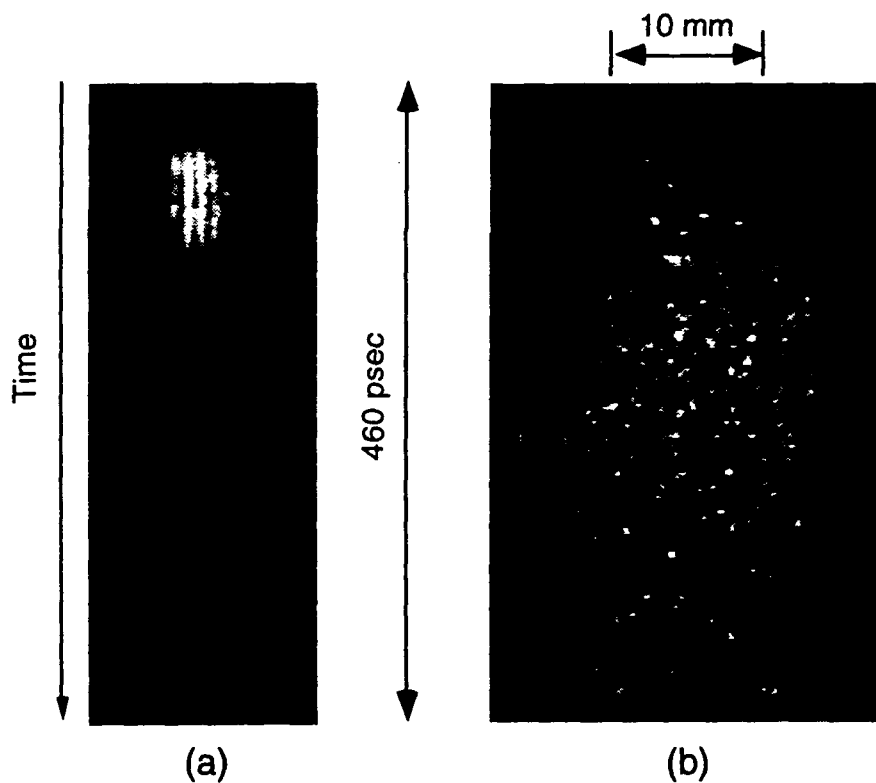


Figure 17. Streak camera images of a resolution bar chart illuminated by a 250  $\mu\text{J}$  Stokes pulse. The streak camera profile (a) shows the 1-dimensional bar image in time without any scatterer present after the bar chart. Profile (b) is the streak camera image produced when the resolution bar chart was placed behind a 5 cm long cell containing 0.364  $\mu\text{m}$  diameter latex spheres in a suspension of ethanol.



We obtained time-gated images from our scattering samples at various relative timings between the input-Stokes light and the pump pulse in the Raman amplifier. An example of a set of these images is shown in Fig. 18 for a solution of polystyrene spheres at a concentration of  $\mu_t \approx 0.56 \text{ mm}^{-1}$ . These data were taken using the  $316 \text{ }\mu\text{m}$  period bars and the Fourier transform of the bar chart was imaged into the Raman amplifier cell. The top set of images, Figs. 18(a)-(d), are taken with a single laser shot, and the lower set of images, Figs. 18(e)-(h), are an average of 16 laser shots. The camera exposure was controlled by adjusting neutral density filters in the amplified Stokes beam. At a relative timing for which the peak of the pump pulse preceded the peak of the Stokes pulse by approximately 9 psec [Figs. 18(a) and 18(e)], no bar chart image was produced and the only signal seen was characteristic of amplified quantum noise. An amplified bar chart image was obtained, however, for relative timings in which the peak of the Stokes pulse overlapped the peak of the pump pulse or led the peak of the pump pulse by up to approximately 50 psec. An example is shown in Figs. 18(b) and 18(f) where the Stokes pulse led the pump by approximately 33 psec. At lead times greater than about 40 psec, the bar chart image degraded in quality until it was not evident in the amplified Stokes signal. An example of this is shown in Figs. 18(c) and 18(d), and more clearly in Figs. 18(g) and (h). The separation time between the Stokes and the pump pulses was increased to 42 and 93 psec, respectively, for those images. Amplified, scattered signal without an image of the bars could be obtained above the amplified quantum noise level for Stokes-to-pump lead times up to 460 psec.

We also obtained time-gated images from samples of non-dairy creamer. At the maximum concentration of  $\mu_t \approx 0.66 \text{ mm}^{-1}$  an average of 64 laser pulses were needed to form good images. Again, no bar chart image was seen at a relative timing for which the pump pulse preceded the Stokes pulse by approximately 9 psec. An amplified bar chart image was produced only for relative timings for which the peak of the Stokes pulse led the peak of the pump pulse by 8 to 25 psec. For Stokes-pulse lead times greater than about 25 psec, no bar chart image was produced in the amplified Stokes signal. For the non-dairy creamer an amplified scattered signal without an image of the bars was detectable above the amplified quantum noise for Stokes-to-pump lead times of up to 430 psec.

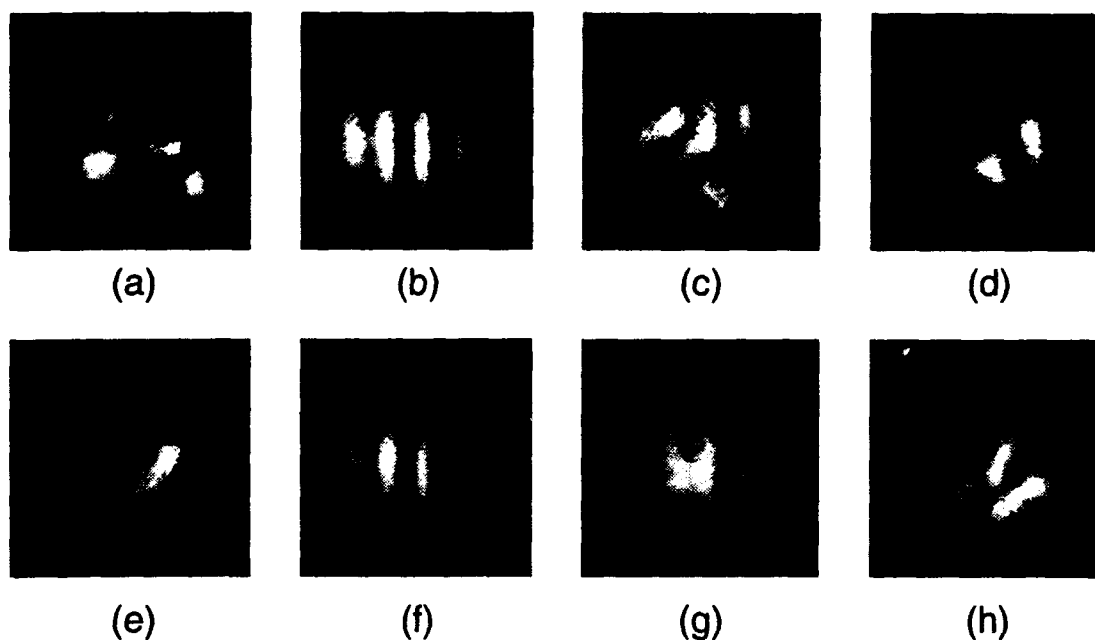


Figure 18. Images of time-gated, amplified Stokes light that has passed through a resolution bar chart and a 5 cm long cell filled with  $0.364\ \mu\text{m}$  diameter latex spheres in a suspension of ethanol. The images in (a) - (d) were produced with a single shot, and the images in (e) - (h) with an integration of 16 shots. The timing of the Stokes pulse relative to the pump pulse was changed for each image, with the peak of the Stokes pulse lagging the peak of the pump pulse by 9 psec in (a) and (e), and advanced relative to the peak of the pump for all other images: 33.5 psec in (b) and (f), 42 psec in (c) and (g), and 93 psec in (d) and (h).

#### DISCUSSION OF RESULTS FOR IMAGING THROUGH SCATTERING MEDIA

Comparison of the results from the linear scattering measurements and the time-gated amplification for the latex spheres are consistent with the conclusion that the image in Figs 18(b) and 18(f) are carried dominantly by light that is transmitted through the sample without scattering. The total attenuation of  $\sim e^{-28}$  for the direct transmission combined with our initial illumination level of  $250\ \mu\text{J}$  gives a transmitted energy of a few photons per amplifier mode, which we have previously determined to be the limit of our sensitivity.<sup>35</sup>

A similar comparison for the results obtained with the non-dairy creamer leads to a different conclusion. Here the scattering measurements indicate an attenuation of  $e^{-33}$  for the unscattered light, which reduces the unscattered intensity below our minimum detection level. We therefore conclude that the time-gated images of the resolution bar chart we obtained at the highest concentrations in non-dairy creamer are due to light that has been forward scattered. This conclusion is supported by the distribution of intensity in the amplified images as a function of relative timing

between the pump and Stokes pulses. The peak intensity in the scattered tail is measured to be four times that of the brightest image in the early part of the pulse, indicating that the component of the light in the scattered tail that is accepted by the Raman amplifier contained more energy than that in the image-bearing component. Under these conditions the image would not be visible without the time gating provided by the Raman amplifier. This result is verified by the inability to see any modulation of the image intensity when viewed by a conventional, low-light-level CCD camera.

In summary, we have demonstrated the use of time-gated, stimulated Raman image amplification to obtain images through scattering media consisting of suspensions of both latex spheres and non-dairy creamer. The results indicate that, in the case of the non-dairy creamer, the image-bearing component contained only a small fraction of the total scattered energy and was composed of forward scattered rather than unscattered light. For the densest scatterers used, images were obtained with the Raman image amplifier, but not with streak cameras or time-integrating cameras. Using available technology this technique can produce images with  $10^4$  -  $10^5$  resolution elements and temporal resolutions in the 1 psec to 100 fsec range, parameters appropriate for imaging through animal tissue.

### Imaging through tissue with time-gated optical systems

Imaging through human tissue with light at visible or near infrared wavelengths offers the potential for cancer screening and detection without the dangers of x-rays. Initially, this optical technique is expected to be used along with x-ray mammography for detection of breast cancers. When a cancerous tumor is detected using x-rays, subsequent non-threatening diagnosis can be made using laser illumination to see the region with more sensitivity and resolution. Image contrast between fibrous tissue and tumors will be present if there is discrimination due to a difference in absorption coefficient or scattering coefficient of the rapidly dividing cells of the tumor as compared with the surrounding normal tissue, causing the tumors to appear either darker or lighter in transmission than the surrounding normal tissue. The difficulties of imaging through the human breast in transillumination are generally thought of as being due to a combination of absorption and scattering, with the latter being the dominant problem. Temporal gating of the transmitted light to reject light that has been delayed due to multiple path scattering has been demonstrated to allow imaging of small objects hidden by, or immersed in, a scattering medium. Several techniques, both electronic and optical, have been proposed and demonstrated to obtain such time-gated images, and similar techniques have been proposed for transillumination of the human breast. Optical techniques will have certain common requirements in breast imaging due to the limitations on the allowed optical irradiation levels on skin.

In considering conditions that will be encountered in time-gated transillumination for breast imaging, one of the main parameters that drives the characteristics of the illumination system is the

fraction of light that is transmitted in the image-bearing component of the light. The ballistic, or unscattered component of the transmitted light, will carry diffraction-limited optical quality but the diffusely scattered light will carry degraded image information. For problems of biological interest, the scattering particles generally have a distribution of sizes with an average value that is larger than the wavelength. We have found that adominal fat is characterised by tight packing of 50  $\mu\text{m}$  diameter fat globules. Thus, there is expected to be minimal effect on the scattering parameters over the wavelength range of 600 nm - 1.2  $\mu\text{m}$  which is the available spectral window between the haemoglobin absorption cut-off at the short wavelength end and water absorption at the higher wavelength end. For purposes of illustration, we expect the absorption coefficient  $\mu_a$  to be about a factor of 100 smaller than the scattering coefficient  $\mu_s = 35 \text{ mm}^{-1}$  (human glandular breast; Peters et. al.) which would indicate that the transmitted fraction of light  $= e^{-\mu_s L}$  in the unscattered or ballistic component of light would be undetectable. Hence, the only hope is to be able to extract a degraded image from the multiply scattered light. The multiple scattering is characterized by a transport length,  $l_t$ , which is related to the scattering length,  $l_s$ , by  $l_t = l_s / (1 - g)$ , where  $g$  is the anisotropy factor. For typical biological materials and optical wavelengths in the near infrared,  $g \sim 0.9$ . Typical values of  $l_t$  are of the order of 1-2 mm.<sup>14</sup>

The required illumination levels can be within the maximum ANSI (American National Standards Institute) standards for single or multiple pulse exposure, depending on the detailed characteristics of the gating techniques and the illumination system. A second characteristic is that the intensity of the light transmitted through the breast from a single pulse of light is likely to be near or below the single photon level. Thus it is desirable to have time gates that are both highly efficient in order to avoid the introduction of excess loss in the system which would further reduce the transmitted light level, and also highly sensitive, to be able to detect light at the photon level. In addition the system should be capable of working at minimal noise levels. These are important considerations since special techniques must be used to provide gating times in the picosecond time regime, and they have varying amounts of loss, sensitivity and inherent noise.

Some quantities that are of interest in characterizing a breast imaging system are the single and multiple pulse illumination levels and the desired signal-to-noise ratio in the image. Other factors which put constraints on the problem concern spatial resolution, field of view and number of resolution elements in the picture, and the fractional transmission of the image-bearing component of the light through the breast. We estimate the required illumination level in terms of these quantities and the number  $N_T$ , of transmitted photons per pixel per laser pulse:

$$E_0 = N_T h\nu / T \Delta x \Delta y$$

where  $E_0$  is the illumination level in  $\text{Joules/cm}^2$ ,  $h\nu$  is the photon energy and is given by Planck's constant  $h$  and the frequency of the light  $\nu$ ,  $T$  is the fraction of transmitted light, and  $\Delta x$  and  $\Delta y$  are the

spatial resolution of an individual pixel. If we use a repetitively pulsed illumination system, the total illumination over the full exposure time is given by

$$E_{0,tot} = (ft)N_T h\nu / T \Delta x \Delta y,$$

where  $f$  is the repetition frequency in  $\text{sec}^{-1}$  and  $t$  is the total exposure time in sec. Another important quantity to be considered is the signal-to-noise ratio in the resulting picture. For the single pulse this can be estimated as  $S/N = N_T/N_N$ , where  $N_N$  is the number of noise photons per pixel accumulated over a single pulse viewing time. The signal-to-noise ratio for the multiple pulse system will grow as either the number of pulses or the square root of the number of pulses.

### Allowable tissue irradiation levels for various laser pulse durations

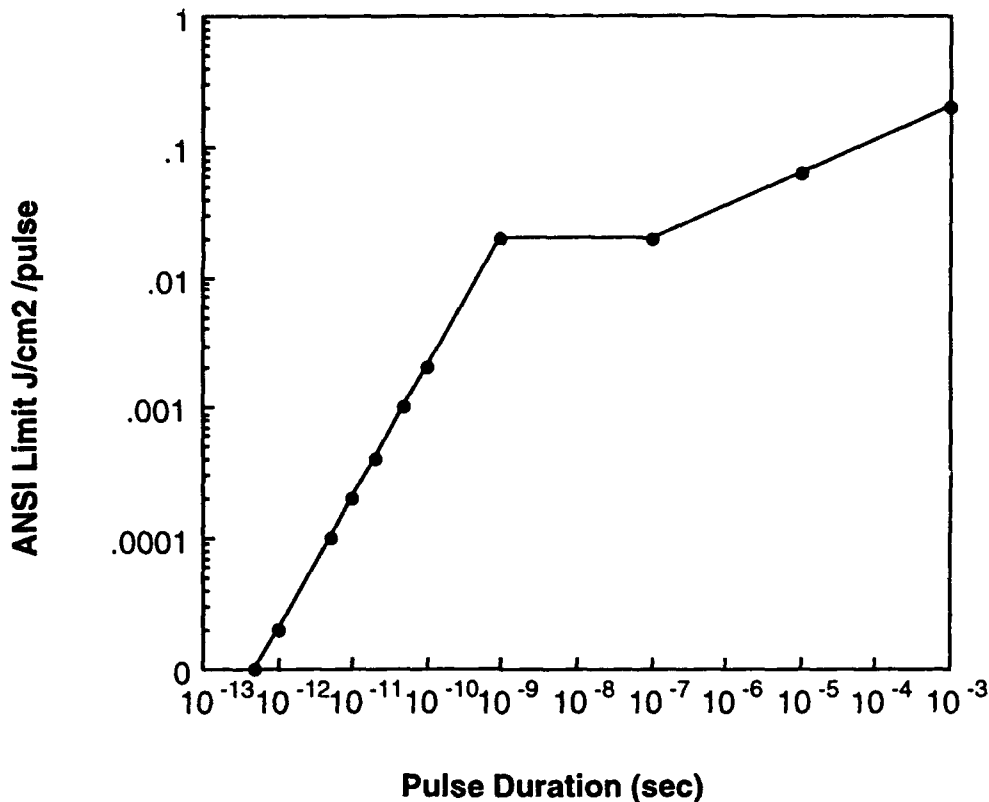


Figure 19. Graphical representation of the ANSI limits for allowable energy density ( $\text{J}/\text{cm}^2$ ) incident on human tissue between 400 and 700 nm versus the laser pulse duration.

According to the the manual: "Safety with Lasers and Other Optical Sources" by D. Sliney and M. Wolbarsht, the maximum allowable energy density per pulse incident on human tissue between 400 and 1400 nm is given to be  $0.02 C_A \text{ J}/\text{cm}^2/\text{pulse}$  for pulse durations of 1-100 ns and to vary as  $1.1 C_A^{4+t}$  for pulse duration,  $t$  in the range of 100 ns to 1s. The correction factor  $C_A = 1$  for

wavelength between 400 and 700nm and increases linearly to 5 at 1050nm. For pulses shorter than 1 ns the advice from the office of the authors is to take the intensity to be constant, that is, the allowable energy density scales inversely with pulse duration. The ANSI standards for energy density exposure are shown graphically in Figure 19 for single laser shots as a function of laser pulse duration.

For multiple pulse irradiation, the allowable number of total pulses  $N_A$  is furthermore limited by the equivalent energy density that a pulse would have if it were of duration equal to  $N_A$  divided by the laser repetition rate,  $f$ . We set the total exposure time to 10s as a practical measure and the ANSI limit for 10s was found by extrapolation. For a given laser pulse duration this then determines the maximum laser repetition rate and hence the number of shots per exposure consistent with irradiation at the ANSI standard. Then, within the allowable radiation exposure levels and considering a given scattering attenuation in a given thickness of tissue, the minimum resolvable linear size is determined. For the lowest transmitted signals the imaging is expected to be at the single photon level and the geometry of the system would be optimised for a noise level of 1 noise photon per resolution element.

## VI. Real-time imaging of debris in oil

A further set of imaging experiments which we addressed, concerned the imaging of metallic or ceramic debris in flowing engine or gear box oil. This problem presents a different set of constraints compared with the turbid scatterers considered above. The objective is to be able to image obscuring particulate matter in a flowing oil system as a diagnostic of engine wear or to give a warning of impending engine failure. Such debris comes from a bearing or gear failure and must be detected on a single pass flow since it is subsequently filtered out in 2-15  $\mu\text{m}$  filter units, in place on most systems. Most bearing materials currently in use are magnetic, or, at least, metallic and can be detected using magnetic chip detectors or inductance circuitry. This will not be the case, however, with newer bearing materials, such as silicon nitride. In addition, techniques currently used do not give information on the number or shape of the debris particles. The new laser imaging technique which we started to develop under this contract is shown schematically in Fig. 20.

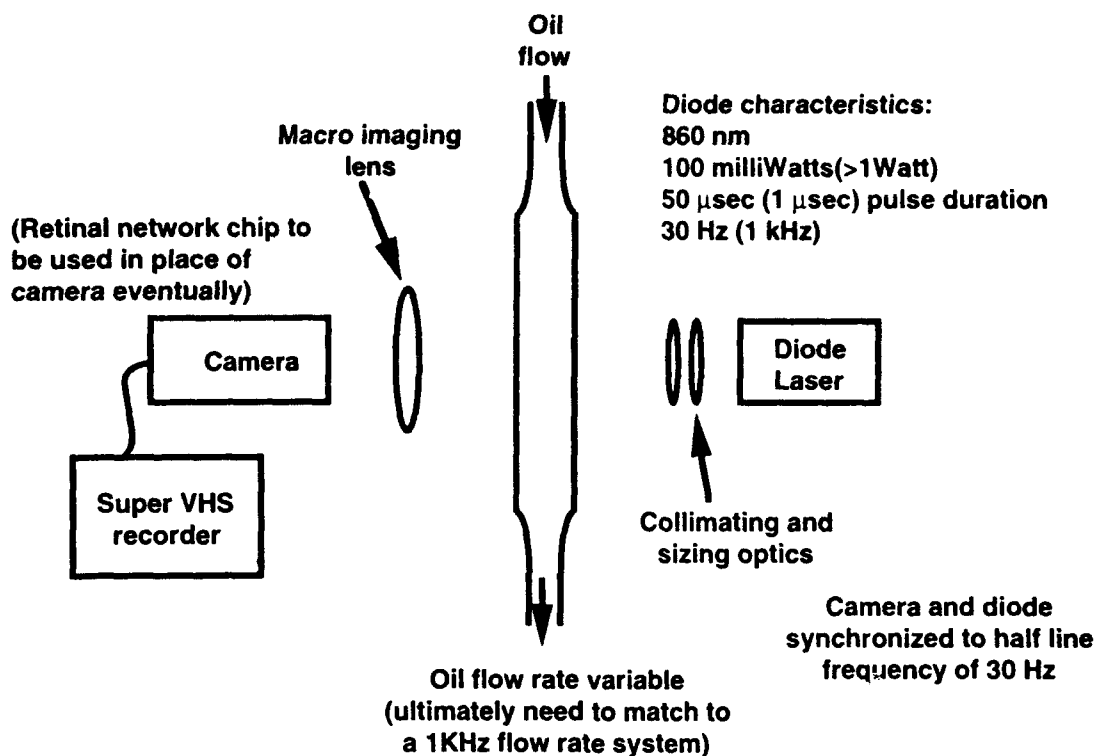


Fig. 20 Schematic of experiment to image debris in flowing oil system.

It is envisioned that a near infra-red diode laser of pulse duration 1  $\mu$ sec and repetition rate 1 kHz be used to image through a 3/4 inch square section of oil pipe, transverse to the oil flow direction. The laser pulse duration is set by the dictated engine oil flow rate so that an image will not appear to be smeared on the camera during the exposure. The repetition rate is set by the requirement that every volume of the oil be sampled. Initial experiments were done using the equipment shown in Fig. 20. A system with a higher resolution camera was used on a test stand oil flow at Tedeco near the end of the contract period. Initial experiments were all done using CCD cameras. Since the commercial market for cameras is driven by the video market, inexpensive CCD cameras are readily available but the output video signal is read as two fields interlaced at 60 Hz. Thus, using pulsed laser systems the destructive-read of each field reduces the potential resolution by a factor of 2 when using the commercial CCD cameras. In addition, the VCR recorders only have a resolution of about 200 - 300 lines unless a super VHS system is used when 400 vertical lines can be stored. Very recently, cameras have appeared with on-chip storage of both fields which are subsequently read out at 30 Hz. Such a camera was used on the oil flow test stand at Tedeco. The Cohu 8420 camera, for instance, has 1134 x 486 active pixels of individual size 8  $\mu$ m x 10  $\mu$ m and so should be able to distinguish a 50  $\mu$ m debris chip from a machining curl. Air bubbles entrained in the hot flowing oil could obscure a debris chip and so a two way viewing arrangement is also envisioned for this project in the future. Ultimately, a retinal network chip will replace both the camera and VCR. The retinal net will be

capable of learning what constitutes normal oil flow and be able to resolve debris and identify abnormal components of the flow.



Fig. 21 Examples of images containing bubbles and synthetic metallic chips, viewed in transmission through a 1cm path of flowing oil.



## References

1. M. D. Duncan, R. Mahon, L. L. Tankersley, and J. Reintjes, *J. Opt. Soc. Am. B*, **5**, 37 (1988).
2. J. Reintjes, M. D. Duncan, R. Mahon, G. Calame, L. L. Tankersley, in *Technical Digest of the 1987 Conference on Lasers and Electro-Optics* (Optical Society of America, Washington, D. C., 1987), p. 184.
3. J. Reintjes, M. D. Duncan, G. Calame, R. Mahon, L. L. Tankersley, in *Technical Digest of the 1988 Conference on Lasers and Electro-Optics, Vol. 7* (Optical Society of America, Washington, D. C., 1988), p. 252.
4. J. Reintjes, G. Calame, M. D. Duncan, R. Mahon, and L. L. Tankersley, in *Optical Phase Conjugation, Raman Beam Cleanup and Adaptive Optics*, Vol. 874, Robert A. Fisher, ed. (SPIE - The International Society for Optical Engineering, Bellingham, Washington, 1988), pp. 87-94.
5. J. R. Ackerhalt and N. A. Kurnit, *Phys. Rev. A* **36**, 1720 (1987).
6. M. A. Greiner-Mothes and K. J. Witte, *Appl. Phys. Lett.* **49**, 4 (1986).
7. L. R. Marshall and J. A. Piper, *Opt. Lett.* **15**, 1345 (1990).
8. D. von der Linde, M. Maier and W. Kaiser, *Phys. Rev.* **178**, 11 (1969).
9. J. H. Newton and G. M. Schindler, *Optics Lett.* **6**, 125 (1981).
10. R. B. Andreev *et al.*, *Sov. J. Quantum Electron.* **12**, 35 (1982).
11. J. R. Ackerhalt, *Phys. Rev. Lett.* **46** 922 (1981).
12. B. Bobbs and C. Warner, *IEEE J. Quantum Electron.* **24**, 660 (1988).
13. V. S. Butylkin *et al.*, *Sov. J. Quantum Electron.* **7**, 867 (1977).
14. J. L. Carlsten, J. M. Telle and R. G. Wenzel, *Opt. Lett.* **9**, 353 (1984).
15. R. G. Wenzel and J. M. Telle, *J. Opt. Soc. Am. B* **3**, 1483 (1986).
16. M. D. Duncan, R. Mahon, L. L. Tankersley, J. Reintjes, *Opt. Comm.* **86**, 538 (1991).
17. M. G. Raymer, I. A. Walmsley, J. Mostowski and B. Sobolewska, *Phys. Rev. A*, **32**, 332 (1985).
18. C. M. Bowden and J. C. Englund, *Optics. Comm.*, **67**, 71(1988).
19. M. D. Duncan, R. Mahon, L. L. Tankersley, and J. Reintjes, *J. Opt. Soc. Am. B*, **8**, March (1991).
20. M. D. Duncan, R. Mahon, L. L. Tankersley, and J. Reintjes, *J. Opt. Soc. Am. B*, **7**, 1336 (1990).
21. Bruce W. Shore, *The Theory of Coherent Atomic Excitation*, Vol. 1, chapter 9, John Wiley & Sons (New York), 1990.
22. D. C MacPherson, R. C. Swanson, and J. L. Carlsten, *Phys. Rev. Lett.*, **61**, 66(1988).
23. S. Andersson-Engels, R. Berg, S. Svanberg, and O. Jarlman, *Opt. Lett.*, **15**, 1179 (1990).
24. J. C. Hebden, R. A. Kruger and K. S. Wong, *Appl. Opt.*, **30**, 788 (1991).
25. J. C. Hebden, *Opt. Lett.* **17**, 444 (1992).
26. L. Wang, P. P. Ho, Y. Liu, G. Zhang and R. R. Alfano, *Science*, **253**, 769 (1991).
27. B. B. Das, K. M. Yoo, and R. R. Alfano, *Opt. Lett.*, **18**, 1092 (1993).

28. J. C. Hebden and R. A. Kruger, SPIE, **1443**, 294 (1991); Med. Phys. **17**, 41 (1990).
29. D. Huang, E. A. Swanson, C. P. Lin, J. S. Schuman, W. G. Stinson, W. Chang, M. R. Hee, T. Flotte, K. Gregory, C. A. Puliafito, and J. G. Fujimoto, Science **254**, 1178 (1991).
30. M. R. Hee, J. A. Izatt, J. M. Jacobson and J. G. Fujimoto, Opt. lett., **18**, 950 (1993).
31. H. Chen, Y. Chen, D. Dilworth, E. Leith, J. Lopez, and J. Valdmantis, Opt. Lett., **16**, 487 (1991).
32. E. Leith , H. Chen, Y. Chen, D. Dilworth, J. Lopez, R. Masri, J. Rudd, and J. Valdmantis. Appl. Opt., **30**, 4204 (1991).
33. K. G. Spears, J. Serafin, N. H. Abramson, X. Zhu and H. Bjelkhagen, IEEE Trans. Biomed. Eng. **36**, 1210 (1989).
34. C. F. Bohren and D. R. Huffman, (Wiley , NY 1983).
35. M. D. Duncan, R. Mahon, L. L. Tankersley, and J. Reintjes, J. Opt. Soc. Am. B, **9**, 2107 - 2121 (1992).